

PDRs4All

XII. FUV-driven formation of hydrocarbon radicals and their relation with PAHs

J. R. Goicoechea¹, J. Pety^{2,3}, S. Cuadrado¹, O. Berné⁴, E. Dartois⁵, M. Gerin³, C. Joblin⁴, J. Klos^{6,7}, F. Lique⁸,
 T. Onaka⁹, E. Peeters^{10,11,12}, A. G. G. M. Tielens^{13,14}, F. Alarcón¹⁵, E. Bron¹⁶, J. Cami^{10,11,12}, A. Canin⁴,
 E. Chapillon^{17,2}, R. Chown^{10,11,18}, A. Fuente¹⁹, E. Habart²⁰, O. Kannavou²⁰, F. Le Petit¹⁶, M. G. Santa-Maria^{21,1},
 I. Schroetter⁴, A. Sidhu^{10,11}, B. Trahin²⁰, D. Van De Putte^{10,11}, and M. Zannese²⁰

(Affiliations can be found after the references)

Received 9 December 2024 / Accepted 5 March 2025

ABSTRACT

The infrared emission from polycyclic aromatic hydrocarbons (PAHs), along with emission from atomic carbon and simple hydrocarbons, is a robust tracer of the interaction between stellar far-UV (FUV) radiation and molecular clouds. We present subarcsecond-resolution ALMA mosaics of the Orion Bar photodissociation region (PDR) in [C I] 609 μm ($^3\text{P}_1\text{--}^3\text{P}_0$), C_2H ($N=4\text{--}3$), and C^{18}O ($J=3\text{--}2$) emission lines, complemented by JWST images of H_2 and aromatic infrared band (AIB) emission. We interpret this data using up-to-date PDR and radiative transfer models, including high-temperature C_2H ($X^2\Sigma^+$)– $o/p\text{-H}_2$ and C (^3P)– $o/p\text{-H}_2$ inelastic collision rate coefficients (the latter, computed by us up to 3000 K). The rim of the Bar shows very corrugated, filamentary, and turbulent structures made of small-scale H_2 dissociation fronts (DFs). The [C I] 609 μm emission peaks very close (≤ 0.002 pc) to the main H_2 -emitting DFs, suggesting the presence of gas density gradients. These DFs are also bright and remarkably similar in C_2H emission, which traces ‘hydrocarbon radical peaks’ characterized by very high C_2H abundances, reaching up to several $\times 10^{-7}$. The high abundance of C_2H and of related hydrocarbon radicals, such as CH_3 , CH_2 , and CH , can be attributed to gas-phase reactions driven by elevated temperatures, the presence of C^+ and C , and the reactivity of FUV-pumped H_2 . The hydrocarbon radical peaks roughly coincide with maxima of the 3.4/3.3 μm AIB intensity ratio, a proxy for the aliphatic-to-aromatic content of PAHs. This implies that the conditions triggering the formation of simple hydrocarbons also favor the formation (and survival) of PAHs with aliphatic side groups, potentially via the contribution of bottom-up processes in which abundant hydrocarbon radicals react *in situ* with PAHs. Ahead of the DFs, in the atomic PDR zone (where $[\text{H}] \gg [\text{H}_2]$), the AIB emission is brightest, but small PAHs and carbonaceous grains undergo photo-processing due to the stronger FUV field. Our detection of trace amounts of C_2H in this zone may result from the photoerosion of these species. This study provides a spatially resolved view of the chemical stratification of key carbon carriers in a PDR. Overall, both bottom-up and top-down processes appear to link simple hydrocarbon molecules with PAHs in molecular clouds; however, the exact chemical pathways and their relative contributions remain to be quantified.

Key words. ISM: abundances – ISM: Molecules, Molecular data, Molecular processes — photon-dominated region (PDR)

1. Introduction

Far-UV radiation (FUV; $6 < E < 13.6$ eV) from massive stars penetrates their natal giant molecular clouds (e.g., Goicoechea et al. 2015; Santa-Maria et al. 2023), heating the gas and dust, altering their chemistry, and driving flows that photoevaporate the cloud (e.g., Maillard et al. 2021). The interaction of FUV radiation and interstellar matter occurs in ‘photodissociation regions’ (PDRs, e.g., Wolfire et al. 2022), where FUV radiation regulates the heating, ionization, and chemistry. PDRs release bright infrared (IR) emission: both collisionally excited and FUV-pumped molecular hydrogen (H_2) line emission as well as aromatic infrared band emission (AIB), which mainly results from IR fluorescence of FUV-pumped polycyclic aromatic hydrocarbons (PAHs, Leger & Puget 1984; Allamandola et al. 1985). PAHs in PDRs lock up as much as 10% of interstellar carbon (e.g., Tielens 2008).

Carbon is an abundant cosmic element (Asplund et al. 2009). Due to its allotropy, simple hydrocarbon molecules are the building blocks of carbon chemistry in space. They participate in the formation of complex organic molecules, PAHs, and carbonaceous grains (Jones 2012). With an ionization potential of 11.3 eV (lower than that of hydrogen), carbon ions (C^+) play a pivotal role in cooling FUV-irradiated neutral gas via the [C II] 158 μm line (Dalgarno & McCray 1972). Additionally, C^+ initiates the carbon chemistry of FUV-irradiated H_2 gas (Stecher & Williams

1972; Freeman & Williams 1982; Tielens & Hollenbach 1985; Sternberg & Dalgarno 1995; Agúndez et al. 2010), triggering the formation of carbon hydrides (e.g., Gerin et al. 2016). Dust extinction and gas absorption progressively reduce the flux and energy of FUV photons inside PDRs (Flannery et al. 1980; Goicoechea & Le Bourlot 2007). At a given cloud depth, depending on FUV flux (G_0) and gas density (n_{H}), the dominant gas-phase carbon reservoir transitions from C^+ to C to CO . These key transformations take place in the so-called $\text{CO}/\text{C}/\text{C}^+$ transition zone of a PDR (e.g., Tielens & Hollenbach 1985; Sternberg & Dalgarno 1995; Goicoechea & Le Bourlot 2007).

The AIB emission at 3.3, 6.2, 7.7, 8.6, 11.2, and 12.7 μm is a specific tracer of PDR environments, and dominates the IR spectra of many galactic sources and star-forming galaxies (Tielens 2008). The observed changes in AIB emission in these sources suggest that the species responsible for this emission undergo changes and photochemical modifications (Peeters et al. 2002). Much of the PAH photoprocessing is controlled by the ratio of the FUV flux to H atom density, $G_0/n(\text{H})$ (Montillaud et al. 2013; Andrews et al. 2016). Observational evidence shows that close to PDR edges, the smallest PAHs are destroyed and the aliphatic content of the AIB carriers is reduced (e.g., Joblin et al. 1996; Peeters et al. 2024; Chown et al. 2024).

Our understanding of the formation, destruction, and reactivity of PAHs is rapidly evolving but is not settled. Some studies

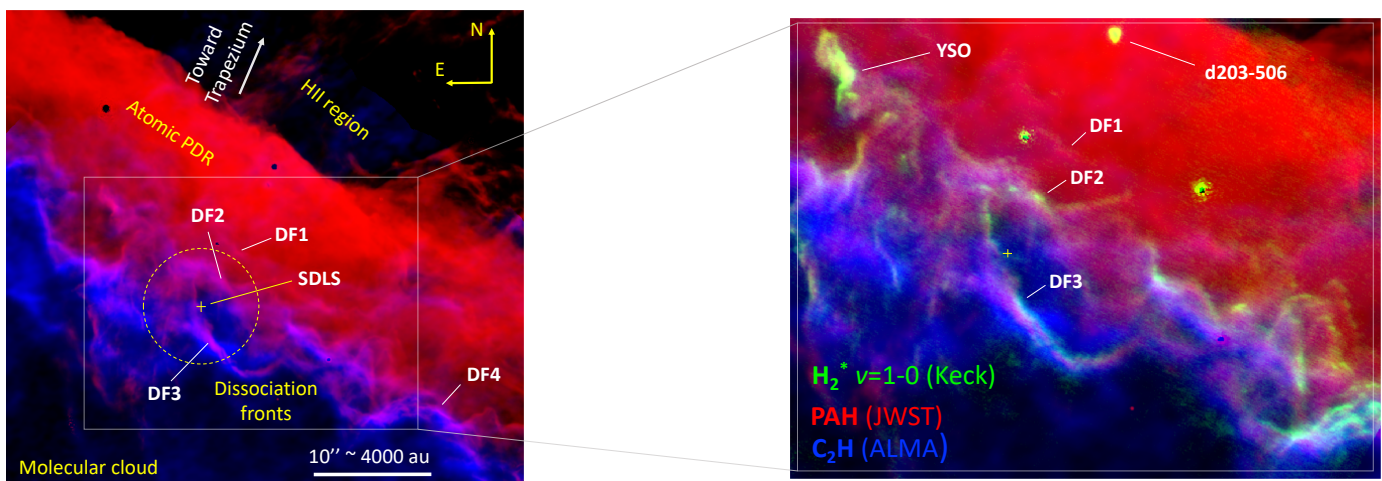


Fig. 1. Subarcsecond view of the Orion Bar PDR. *Left:* ALMA C_2H $N=4-3$ line emission (blue) and JWST F335M–F330M image (red), a proxy of the ~ 3.3 μm AIB feature (Habart et al. 2024). For reference, we show the IRAM 30 m single-dish line survey position (SDLS) at $\alpha(2000) = 5:35:20.8$ and $\delta(2000) = -05:25:17$ with a dashed circle centered at the yellow cross. *Right:* Zoom to a smaller field adding a Keck H_2 $v=1-0$ $S(1)$ image (green) from Habart et al. (2023). Table A shows the coordinates of the main dissociation fronts discussed in this work.

suggest that PAHs form through the photoprocessing of very small carbonaceous grains (e.g., Cesarsky et al. 2000; Berné et al. 2007; Pilleri et al. 2012). This is a ‘top-down’ mechanism. In addition, the recent radio detection in TMC-1 of polar cyano derivatives of small PAHs (McGuire et al. 2018, 2021; Wenzel et al. 2024a,b; Cernicharo et al. 2024) and the detection of indene ($c-C_9H_8$, a very simple asymmetric PAH; Cernicharo et al. 2021) demonstrates that free-flying, gas-phase PAHs exist in dark molecular clouds before star formation (i.e., before FUV processing). This suggests that PAHs already existed and/or that ion-molecule reactions and radical chemistry (e.g., Kaiser et al. 2015; Zhao et al. 2019; He et al. 2020; Lemmens et al. 2022; Levey et al. 2022) contribute to the *in situ* growth of PAHs in cold ($\approx 10-20$ K) gas. The much higher temperatures in PDRs (up to several hundred K), along with the enhanced abundances of simple hydrocarbons triggered by FUV-induced chemistry (starting with CH^+ ; Nagy et al. 2013; Joblin et al. 2018; Goicoechea et al. 2019), may provide another environment for ‘bottom-up’ PAH formation, followed by PAH photoprocessing.

Observations of interstellar PDRs reveal open-shell¹ hydrocarbon radicals such as CH ($^2\Pi$), CH_2 (3B_1), C_2H ($^2\Sigma^+$), $c-C_3H$ (2B_2), $l-C_3H$ ($^2\Pi$), and C_4H ($^2\Pi$), which are highly reactive, as well as closed-shell hydrocarbons, such as CH^+ ($^1\Sigma^+$), $c-C_3H_2$ (1A_1), $l-H_2C_3$ (1A_1), $l-C_3H^+$ ($^1\Sigma^+$), and CH_3^+ (\tilde{X}^1A') (Fuente et al. 2003; Teyssier et al. 2004; Polehampton et al. 2005; Pety et al. 2005, 2012; Pilleri et al. 2013; Guzmán et al. 2015; Cuadrado et al. 2015; Tiwari et al. 2019; Nagy et al. 2015, 2017; Goicoechea et al. 2019; Zannese et al. 2025). The origin of this rich carbon chemistry in such harsh environments is still debated.

Early gas-phase PDR models underestimated the observed abundances of some of these hydrocarbons, especially as the number of carbon atoms increases. In addition, at the moderate angular resolution provided by previous generation telescopes, the AIB and hydrocarbon emission peaks seemed to approximately coincide. This led astronomers to suggest that the high abundances of specific hydrocarbons (that we generally term C_xH_y) could result from the photodestruction of PAHs or very small carbonaceous grains (Fossé et al. 2000; Fuente et al. 2003; Teyssier et al. 2004; Pety et al. 2005; Alata et al. 2015; Guzmán et al. 2015), and there is experimental support for such a link (Jochims et al. 1994; Le

Page et al. 2003; Allain et al. 1996; Joblin 2003; Bierbaum et al. 2011; Alata et al. 2014; Marciniak et al. 2021; Tajuelo-Castilla et al. 2024). However, gas-phase production of hydrocarbons in a PDR may also be linked to the high temperatures and the enhanced reactivity of FUV-pumped H_2 (Cuadrado et al. 2015). With JWST and ALMA, we can spatially resolve the emission from H_2 , PAHs, and simple hydrocarbons, allowing us to accurately link it to the steep physico-chemical gradients in PDRs. This capability can further elucidate these opposing, yet perhaps complementary possibilities, as well as the processes of PAH growth and destruction. This is also a relevant question in the extragalactic context, where the abundance of simple hydrocarbons such as C_2H can be very high in massive star-forming environments exposed to strong irradiation (e.g., Meier et al. 2015; García-Burillo et al. 2017). In this paper we target the Orion Bar, the prototypical strongly irradiated PDR (Fig. 1). In Sect. 2 we introduce the source and observational dataset. In Sect. 3 we discuss the most salient features of the ALMA and JWST spectroscopic-images taken by PDRs4All-Team et al. (2022). In Sect. 4 we analyze these images with emission crosscuts, as well as non-LTE radiative transfer models. In Sect. 5 we model the chemistry of C_2H and related hydrocarbon radicals. Finally, in Sect. 6 we try to find links with the observed AIB emission.

2. Observations

2.1. The Orion Bar PDR

The Orion Bar is an interface of the Orion molecular cloud (OMC-1) and the Huygens H II region (M42) photoionized by massive stars in the Orion Nebula cluster, mainly θ^1 Ori C in the Trapezium (e.g., O’Dell 2001). At an adopted distance of 414 pc (see discussion in Habart et al. 2024), this region is the closest cluster environment with ongoing high-mass star-formation. The Bar is a strongly irradiated PDR (with $G_0 > 10^4$, Marconi et al. 1998; Peeters et al. 2024). The ionization front (IF) at the edge of the Bar marks the transition between the H II region (with $[H^+] \gg [H]$, where $[X]$ refers to the abundance of species X relative to H nuclei) and the neutral and predominantly atomic-gas zone of the PDR, where $[H] \gg [H_2]$ and $n(H) \approx (5-10) \times 10^4 \text{ cm}^{-3}$ (e.g., Tielens et al. 1993; Pellegrini et al. 2009; van der Werf et al. 2013; Habart et al. 2024; Peeters et al. 2024). At $\sim 10-20''$

¹ We give the ground electronic state in parentheses.

(~ 0.02 – 0.04 pc) from the IF, the FUV flux is attenuated enough that $[H_2] \gg [H]$. This is the H_2/H transition zone, or dissociation front (DF), where most of the gas becomes molecular and some structures reach up to $n_H = n(H) + 2n(H_2) \gtrsim 10^6 \text{ cm}^{-3}$ (e.g., Goicoechea et al. 2016). The DF displays a plethora of ro-vibrational H_2 lines (Parmar et al. 1991; Luhman et al. 1994; Allers et al. 2005; Shaw et al. 2009; Kaplan et al. 2021; Peeters et al. 2024; Van De Putte et al. 2024) and AIB emission (Sloan et al. 1997; Chown et al. 2024). In the standard view of a constant-density PDR, the $CO/C/C^+$ transition zone is expected to occur beyond the DF (e.g., Tielens & Hollenbach 1985). However, owing to low-angular resolution, $[C\ II]$ $158 \mu\text{m}$ and $[C\ I]$ $370,609 \mu\text{m}$ observations have not accurately settled the exact position of this zone (e.g., Tauber et al. 1995; Wyrowski et al. 1997; Ossenkopf et al. 2013; Goicoechea et al. 2015; Cuadrado et al. 2019).

2.2. ALMA imaging

We carried out a $\sim 40'' \times 40''$ mosaic of the Bar (Fig. 1) using forty-seven ALMA 12 m antennas at the frequency of the $C_2H\ N=4-3$ ($349.3 \text{ GHz}^2\ N=4-3$), $C^{18}O\ J=3-2$ (329.3 GHz) and $[C\ I]$ $609 \mu\text{m}$ lines (in three different frequency setups). These observations belong to project 2021.1.01369.S (P.I.: J. R. Goicoechea) and consisted of a 27-pointing (C_2H and $C^{18}O$) and 52-pointing ($[C\ I]$ $609 \mu\text{m}$) mosaics centered at $\alpha(2000) = 5^h 35^m 20.6^s$; $\delta(2000) = -05^\circ 25' 20.0''$. We observed the $C_2H\ N=4-3$ and $C^{18}O\ J=3-2$ lines (band 7), as well as the $[C\ I]$ $609 \mu\text{m}$ line (band 8) using correlators providing $\sim 282 \text{ kHz}$ and $\sim 564 \text{ kHz}$ resolution, respectively. We binned all spectra to a common velocity resolution of 0.4 km s^{-1} . The total observation times with the ALMA 12 m array were ~ 2.7 h and 4.6 h, respectively. In order to recover the extended emission (a few tens of arcsec) filtered out by the interferometer, we used ACA 7 m array, as well as fully sampled single-dish maps obtained with the total-power (TP) antennas as zero- and short-spacings.

We calibrated the interferometer data using the standard ALMA pipeline in CASA. We calibrated the TP data and converted it into a position-position-velocity cube also using CASA. Following Rodríguez-Fernández et al. (2008), we used the GILDAS/MAPPING software to create the short-spacing visibilities not sampled by the ALMA-7m and ALMA-12m interferometers:

(i) We first use the TP and ALMA-7m to produce a clean image containing all spatial information from 0 to 30 m, that is, equivalent to a total power telescope of 30 m-diameter. In this step, the TP map is deconvolved from the TP beam in the Fourier plane before multiplication by the ALMA-7m primary beam in the image plane. After a last Fourier transform, we sampled the pseudo-visibilities between 0 and 5 m, the difference between the diameters of the TP and the ALMA-7m antennas. These visibilities were then merged with the ALMA-7m interferometric observations. Each mosaic field was imaged and a dirty mosaic was built combining those fields in the following optimal way in terms of signal-to-noise ratio (Pety & Rodríguez-Fernández 2010). The dirty image was deconvolved using the standard Högbom CLEAN algorithm. The clean image has an elliptical beam that is rounded by smoothing with a Gaussian to the angular resolution corresponding to a telescope of 30 m.

² We refer to the $C_2H\ F=5-4$ and $F=4-3$ hyperfine structure (HFS) lines of the $N=4-3$, $J=9/2-7/2$ fine-structure transition. These two HFS lines overlap and result in a single, unresolved line at $\sim 349.339 \text{ GHz}$. Due to this blending, the resulting line profile may not provide precise line widths if line overlap and opacity effects are significant (different HFS lines can have different excitation temperatures, line opacities, and line widths; e.g., for HCN HFS lines, see, Goicoechea et al. 2022).

(ii) We then used the resulting TP+ALMA-7m image with a typical resolution of $6''$ to create the short-spacing visibilities not sampled by the ALMA-12m interferometer. The TP+ALMA-7m map is deconvolved from the TP+ALMA-7m beam in the Fourier plane before multiplication by the ALMA-12m primary beam in the image plane. After a last Fourier transform, pseudo-visibilities were sampled between 0 and 12 m, the ALMA-12m diameter. In principle, we could have sampled between 0 and 18 m. In practice, the ALMA-12m visibilities above 12 m have a better quality than the one obtained from TP+ALMA-7m above 12 m. These visibilities were then merged with the ALMA-12m interferometric observations and the resulting dataset was deconvolved as in step 1. The resulting data cube was then scaled from $Jy \text{ beam}^{-1}$ flux units to main beam temperature, T_{mb} , scale using the synthesized beam size.

The final synthesized beams are $0.52'' \times 0.38''$ at position angle $PA = 110^\circ$ (492 GHz), $0.78'' \times 0.50''$ at $PA = 48^\circ$ (349.3 GHz), and $0.77'' \times 0.60''$ at $PA = 64^\circ$ (329.3 GHz). This implies nearly a factor ~ 30 better resolution than previous $C_2H\ N=4-3$ and $[C\ I]$ $609 \mu\text{m}$ single-dish maps of the Orion Bar (van der Wiel et al. 2009; Tauber et al. 1995). The typical rms noise of the final cubes are $\sim 0.19 \text{ K}$ (at 349.3 GHz), $\sim 0.24 \text{ K}$ (at 329.3 GHz), and $\sim 0.63 \text{ K}$ (at 492 GHz) per velocity channel.

2.3. JWST and Keck infrared observations: PAHs and H_2

We use JWST IR images of the H_2 and AIB emission obtained and calibrated by PDRs4All-Team et al. (2022). Here we analyze JWST/NIRCam F335M–F330M and F470M–F480M (continuum subtracted) photometric images as proxies of the $3.3 \mu\text{m}$ AIB and $H_2\ v=0-0\ S(9)$ emission, respectively (Habart et al. 2024). The point-spread-function (PSF) FWHM of these images is ~ 0.1 – $0.2''$. We also make use of the narrow-band filter image at $2.12 \mu\text{m}$, dominated by the $H_2\ v=1-0\ S(1)$ line emission, obtained by us using Keck/NIRC2 adaptive optics at $\sim 0.1''$ resolution (Habart et al. 2023). Figure 1 shows a composite RGB image using these images. We further employ near-IR NIRSpec (Peeters et al. 2024) and mid-IR MIRI-MRS mosaics (Chown et al. 2024; Van De Putte et al. 2024). The FoV of these spectroscopic-images is notably smaller, about $27'' \times 6''$, but include the main dissociation fronts and the externally irradiated protoplanetary disk d203-506, observed by us with ALMA and JWST spectrometers (e.g., Berné et al. 2023, 2024; Goicoechea et al. 2024). In addition, we utilize images of the AIB $3.4 \mu\text{m}$ over $3.3 \mu\text{m}$ band ratio inferred with NIRSpec at about $0.1''$ resolution (Peeters et al. 2024). Finally, we use MIRI-MRS images of the low-energy $H_2\ v=0-0$ pure rotational emission lines $S(1)$, $S(2)$, $S(3)$, and $S(4)$ at 17.03 , $12.28 \mu\text{m}$, $9.66 \mu\text{m}$, and $8.02 \mu\text{m}$ respectively. The PSF FWHM of these observations varies between $0.7''$ and $0.3''$.

2.4. IRAM 30 m and Herschel/HIFI multi- $N\ C_2H$ observations

To get a broader view of the Bar and to study beam-dilution effects of single-dish observations, we obtained a $2.5' \times 2.5'$ map of the $C_2H\ N=4-3$ emission over the entire region (see Fig. C.1 in the Appendix), using the IRAM 30 m telescope (Pico Veleta, Spain) with the E330 receiver and the FTS backend at 200 kHz resolution. We carried out on-the-fly scans along and perpendicular to the Bar. The resulting spectra were gridded to a data cube through convolution with a Gaussian kernel providing a final resolution of $\sim 8''$. The total integration time was ~ 6 h during excellent winter conditions ($\lesssim 1 \text{ mm}$ of precipitable water vapor). The achieved rms noise is $\sim 1 \text{ K}$ per resolution channel.

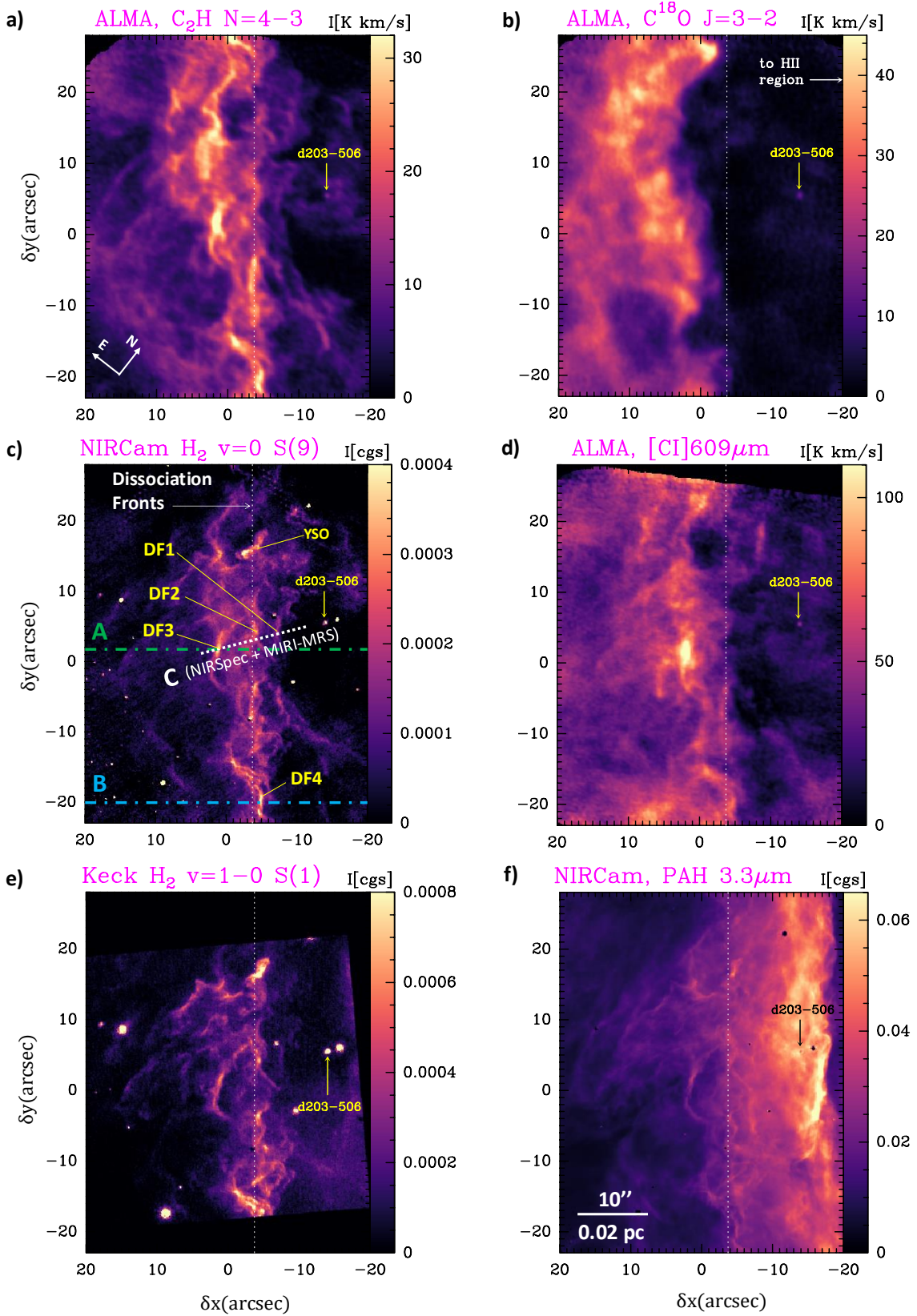


Fig. 2. ALMA, JWST/NIRCam, and Keck images of the Orion Bar PDR. We rotated all images to bring the FUV-illuminating direction from the Trapezium stars in the horizontal direction and from the right. The center of all images is at $\alpha(2000) = 5^{\text{h}}35^{\text{m}}20.50^{\text{s}}$; $\delta(2000) = -05^{\circ}25'21.4''$. The vertical dashed white line marks the approximate position of the main H_2 dissociation fronts parallel to the Bar. (a) $\text{C}_2\text{H } N=4-3$ and (b) $\text{C}^{18}\text{O } J=3-2$. (c) NIRCcam F470M–F480M image, a proxy of the $\text{H}_2 v=0 S(9)$ line at $4.69 \mu\text{m}$ (Habart et al. 2024). Dashed and dotted lines show the position and orientation of the intensity crosscuts A, B (see Fig. 3) and C (the JWST spectroscopy cut, Fig. 7) discussed in the text. (d) $[\text{C } \text{i}] 609 \mu\text{m}$. (e) Keck/NIRC2 image around the $\text{H}_2 v=1-0 S(1)$ line at $2.2 \mu\text{m}$ (Habart et al. 2023). (f) NIRCcam F335MR–F330M image, a proxy of the AIB emission at $3.3 \mu\text{m}$ (Habart et al. 2024). An arrow marks the position of protoplanetary disk d203-506. The units “cgs” refer to $\text{erg s}^{-1} \text{cm}^{-2} \text{sr}^{-1}$. We show more details in the combined RGB images in Fig. C.3 of the Appendix.

To better understand the excitation of C_2H lines and to accurately constrain our PDR models, we complemented our analysis with existing observations of multiple C_2H rotational lines ($N=1-0$ to $4-3$) obtained with the IRAM 30m telescope ($\sim 8''$ to $\sim 28''$ resolution) toward the “single-dish line survey” position (SDLS, see Fig. 1 left) that includes DFs observed with ALMA and JWST, at $\alpha_{2000} = 05^h 35^m 20.8^s$, $\delta_{2000} = -05^\circ 25' 17.0''$. Cuadrado et al. (2015) first presented this data. In addition, we complemented our dataset by including rotationally excited C_2H lines ($N=6-5$ to $N=10-9$) detected by Nagy et al. (2015, 2017) with the Herschel Space Observatory toward the “CO⁺ peak” position (Stoerzer et al. 1995). This position is located at only $\sim 4''$ from the SDLS position. Thus, within the area subtended by the Herschel beams. These observations were carried out with HIFI (de Graauw et al. 2010) at a spectral resolution of 1.1 MHz (0.7 km s^{-1} at 500 GHz). HIFI’s angular resolution ranges from $\sim 20''$ to $\sim 42''$ (Roelfsema et al. 2012).

Because the beam size of the IRAM 30 m and Herschel telescopes varies with frequency, the observation of multiple C_2H rotational lines provides the line intensity averaged over slightly different areas of the Bar. These observations do not spatially resolve the emission arising from the different small-scale dissociation fronts. To approximately correct for these beam-size differences, we estimated a frequency-dependent ‘beam coupling factor’ (f_b) using the spatial information provided by the high-angular resolution C_2H $N=4-3$ map taken with ALMA (see Appendix B).

3. Results

Figure 1 (right panel) shows a RGB image composed of JWST/NIRCam (red, AIB $3.3 \mu\text{m}$; the C–H stretching mode), Keck (green, H_2 $v=1-0$ $S(1)$) and ALMA (blue, C_2H $N=4-3$) observations of the southern edge of the Orion Bar. Labels indicate the main structures and objects in this FoV. The RGB image reveals a very structured dissociation front made of small-scale fronts (see Habart et al. 2024). These fronts are engulfed by a PAH-emitting “halo” that separates the predominantly neutral atomic gas edge of the cloud from the adjacent H II region (hot ionized gas). Figure 2 shows $\sim 40'' \times 40''$ ($\sim 0.08 \text{ pc} \times 0.08 \text{ pc}$) images of multiple tracers individually: (a) C_2H $N=4-3$, (b) $C^{18}O$ $J=3-2$, (c) H_2 $v=0-0$ $S(9)$, (d) [C I] $609 \mu\text{m}$; (e) H_2 $v=1-0$ $S(1)$; and (f) AIB $3.3 \mu\text{m}$. These two H_2 lines originate from high energy levels populated through radiative and collisional de-excitation of FUV-pumped H_2 (Habart et al. 2023; Peeters et al. 2024). In this study, we rotated all images by 37.5° clockwise to bring the FUV illumination from the Trapezium stars in the horizontal direction³. The vertical dotted line marks the approximate position of the main H_2 dissociation front (DF), the H_2/H transition zone of the PDR. To the left of this dotted line, the PDR gas is mostly molecular, meaning $[H_2] \gg [H]$. To the right, the PDR gas is predominantly atomic, with $[H_2] \ll [H]$. This strongly irradiated atomic zone hosts the brightest AIB emission (Habart et al. 2024; Peeters et al. 2024; Chown et al. 2024), an indication of how resistant these aromatic species can be. The DF runs roughly parallel to the ionization front. The rim of the AIB emission delineates the IF, the edge of the H II region.

Instead of a unique H_2/H transition zone, Figs. 2c and 2e show a very corrugated zone composed of multiple small-scale DFs (Habart et al. 2023, 2024; Peeters et al. 2024). These IR H_2 -emitting fronts nearly match the HCO^+ $J=4-3$ structures

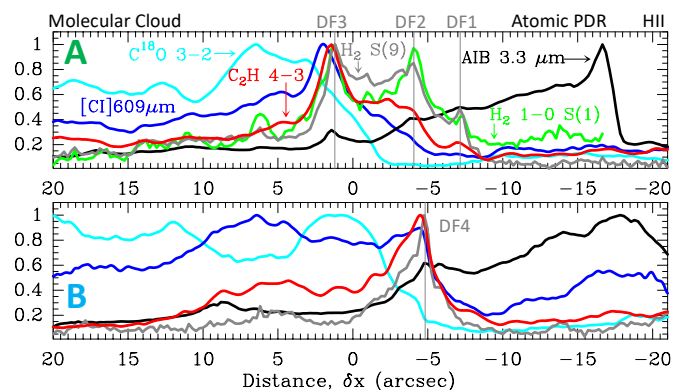


Fig. 3. Vertically-averaged crosscuts A and B perpendicular to the Bar and parallel to the FUV illumination direction (Fig. 2c). Crosscut A (B) passes through $\delta y = +2''$ ($\delta y = -20''$). Both crosscuts have a width of $\Delta(\delta y) = 6''$. Both plots show normalized line intensities.

previously observed by ALMA (Goicoechea et al. 2016). On the other hand, the more FUV-shielded cloud interior (as traced by the optically thin $C^{18}O$ emission) shows a less filamentary but more clumpy morphology, which becomes bright as the IR H_2 emission dims. This implies that the H_2 emission from DF3 and DF4 marks the FUV-irradiated rims of molecular gas structures characterized by bright $C^{18}O$ emission (see also Fig. C.3).

Our ALMA images reveal bright [C I] $609 \mu\text{m}$ emission very close to many H_2 emission peaks (Fig. 2d). In addition, a more diffuse [C I] $609 \mu\text{m}$ emission component exists toward the cloud interior. The ALMA images also reveal bright, filamentary C_2H emission in all small-scale DFs, either very close to or nearly coincident with the H_2 emission (Fig. 2a). Indeed, the spatial distribution of the C_2H emission is well correlated with that of FUV-pumped H_2 (traced by the excited $v=1-0$ $S(1)$ and $v=0-0$ $S(9)$ lines; see Appendix D). In addition, $I(C_2H 4-3)$ is anti-correlated with the $3.3 \mu\text{m}$ AIB emission in the atomic PDR zone, where the AIB emission is much brighter (Appendix D).

The molecular emission in the atomic PDR zone (to the right of the vertical dotted line in Fig. 2) is more difficult to interpret. It can arise from the Bar, but also from the background, from deeper layers of OMC-1 illuminated at a slanted angle. Determining its origin requires an investigation of the line velocity centroid, which may vary among these components (see Sect. 3.2).

3.1. Crosscuts A and B through the PDR

To dissect the typical structures and stratification seen in the PDR, Fig. 3 shows normalized intensity cuts perpendicular to the Bar, extracted from ALMA and IR filter images (Fig. 2c indicates the position of these cuts). We chose two crosscuts passing through $\delta y = +2''$ (cut A) and $\delta y = -20''$ (cut B), roughly parallel to the incoming FUV radiation. The sharp drop in the $3.3 \mu\text{m}$ AIB emission delineates the location of the IF (see Peeters et al. 2024). In cut A, three differentiated (H_2 -bright) DFs appear at $\sim 11''$ (DF1), $\sim 14''$ (DF2), and $\sim 17''$ (DF3) from the IF (at $\sim 0.021 \text{ pc}$, $\sim 0.027 \text{ pc}$, and $\sim 0.033 \text{ pc}$, respectively; see also, Habart et al. 2024; Peeters et al. 2024). DF1 and DF2 show faint [C I] and C_2H emission relative to that of H_2 , and they do not show significant $C^{18}O$ emission. Thus, they appear as filaments that are translucent to FUV radiation. That is, they show H_2 and AIB $3.3 \mu\text{m}$ emission but have low column density perpendicular to the line of sight (no or very little $C^{18}O$). In Sect. 4.2, we infer more details about their geometry and possible origin.

³ We adopt the convention that FUV radiation from the Trapezium stars impinges from the right-hand side of the images. This convention applies to all rotated images and PDR models presented in this paper.

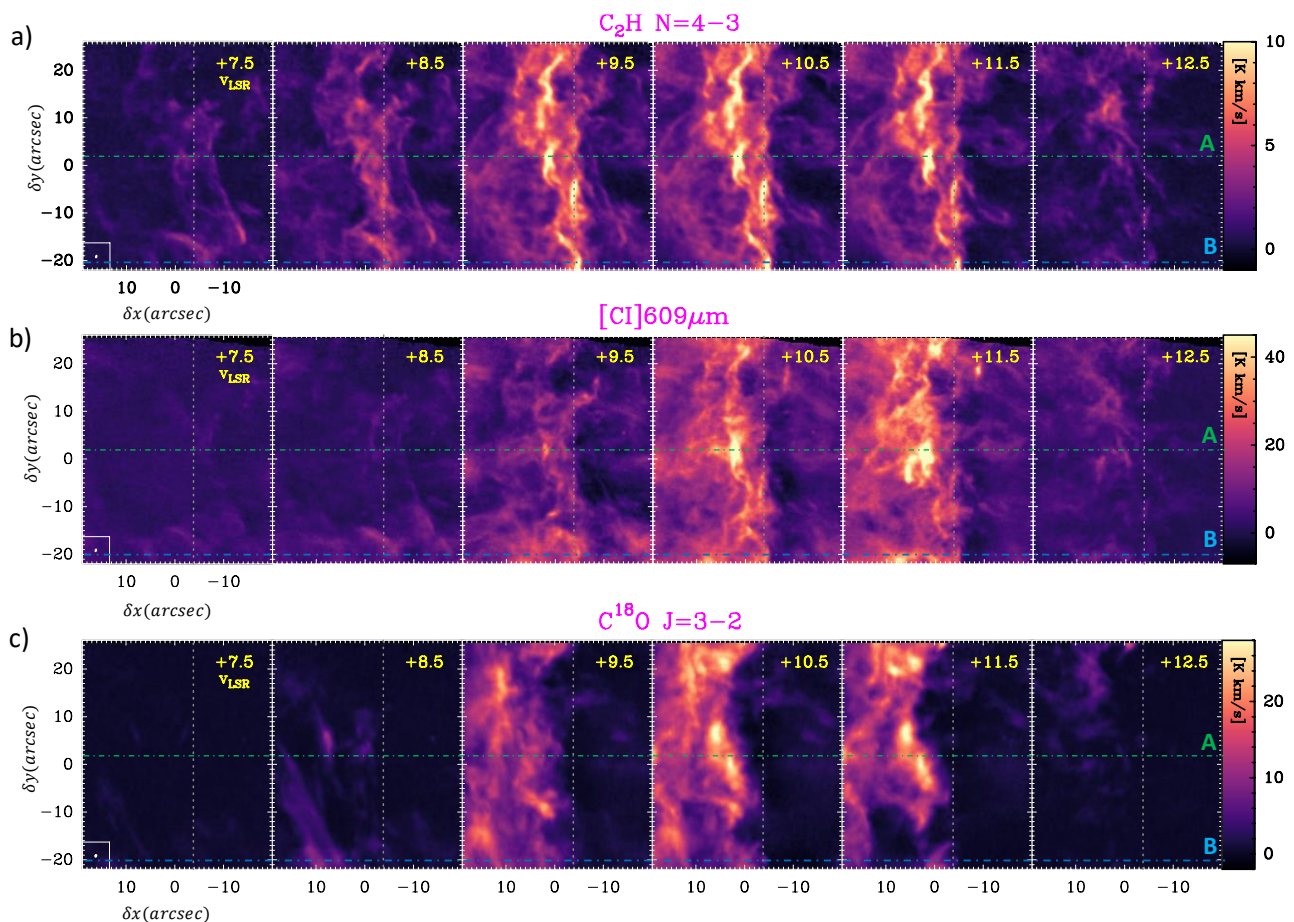


Fig. 4. ALMA velocity channel maps of the Bar, from $v_{\text{LSR}} = +7$ to $+12.5$ km s^{-1} , in bins of 1 km s^{-1} . All images have been rotated to bring the FUV-illuminating direction in the horizontal direction (from the right). The synthesized beam of each mosaic is indicated in the bottom-left corner of the first panel. The vertical dashed white line crosses DF2 ($\delta x \approx -4''$) and marks the approximate position of the main H_2 dissociation fronts parallel to the Bar. The horizontal lines show the position of the vertically-averaged cuts A and B, parallel to the incoming FUV, discussed in the text.

DF3 is different. It is located deeper in the molecular PDR and represents a DF type corresponding to the irradiated rim of a larger molecular gas structure or clump, which is traced by bright C^{18}O emission. The separation between the $[\text{C I}]$ 609 μm and H_2 emission peaks (roughly the separation between the CO/C and H_2/H transition zones) is very small $\lesssim 0.8''$ ($\lesssim 0.002$ $\text{pc} \approx 400$ au) and implies $\Delta A_V \lesssim 0.1$ – 0.2 mag, adopting $n_{\text{H}} \approx (5$ – $10) \times 10^4$ cm^{-3} (as in the atomic PDR zone; Tielens et al. 1993; van der Werf et al. 2013; Peeters et al. 2024) and $A_V/N_{\text{H}} = 3.5 \times 10^{-22}$ mag cm^2 (Cardelli et al. 1989). This width is smaller than the expected separation in a constant-density PDR ($\Delta A_V \approx 1$ – 2 mag; e.g., Tielens & Hollenbach 1985), and suggests higher densities in the molecular PDR compared to the atomic PDR zone.

Cut B shows a single H_2 -bright dissociation front (DF4) that nearly coincides with the bright C_2H emission. This cut shows an even less pronounced spatial stratification. This suggests that DF4 is the rim of a high density structure, more akin to a tilted sheet of FUV-irradiated gas. Deeper into the cloud, cut B reveals moderately bright $[\text{C I}]$ 609 μm emission (i.e., it does not disappear) that follows that of C^{18}O $J = 3$ – 2 at $\delta x > 10''$. This deeper $[\text{C I}]$ 609 μm emission seems to be associated with a secondary peak at $\delta x \approx +7''$. A relevant result for hydrocarbon chemistry is that in all DFs, C_2H peaks ahead of the $[\text{C I}]$ 609 μm emission peak, implying that the observed C_2H emission arises near the $\text{CO}/\text{C}/\text{C}^+$ transition, where the gas is rich in C^+ ions.

3.2. Small-scale gas kinematics

Figure 4 shows C_2H $N = 4$ – 3 (a), $[\text{C I}]$ 609 μm (b), and C^{18}O $J = 3$ – 2 (c) emission in different LSR velocity intervals. These plots dissect the line emission in 1 km s^{-1} channels, from $v_{\text{LSR}} = +7.5$ to $+12.5$ km s^{-1} . They unveil the small-scale structure, both spatially and in velocity, of the molecular gas exposed to strong FUV radiation. They show many C_2H -emitting elongated structures roughly parallel to the IF. The morphological similitude between the H_2 emission and the edge of the C_2H emission suggests that C_2H is a good proxy of the H_2 -emitting gas kinematics (see also next section and Fig. D.1).

Emission from the Bar PDR typically peaks at LSR velocities around $v_{\text{LSR}} \approx 10$ – 11 km s^{-1} (e.g., Cuadrado et al. 2017). The LSR velocity of the OMC-1 emission, in the background, is $v_{\text{LSR}} \approx 8$ – 9 km s^{-1} (e.g., Berné et al. 2014; Goicoechea et al. 2020). Figure 5 shows velocity-resolved line profiles extracted across cut A. The integrated line intensities in DF3 and deeper molecular layers are largely dominated by emission from the Bar (red vertical dashed lines). Some spectra show a minor contribution from a second, faint emission component at $v_{\text{LSR}} \approx 8$ km s^{-1} (blue vertical dashed lines). This faint component becomes more significant in DF1 (at $\delta x \approx -7''$) and it originates from gas in OMC-1, in the background, or from gas structures behind the PDR, likely the base of the cloud escarpment that forms the Bar. A two-Gaussian fit to the $[\text{C I}]$ 609 μm spectra (where the two components are more clearly seen) reveals that the velocity centroid

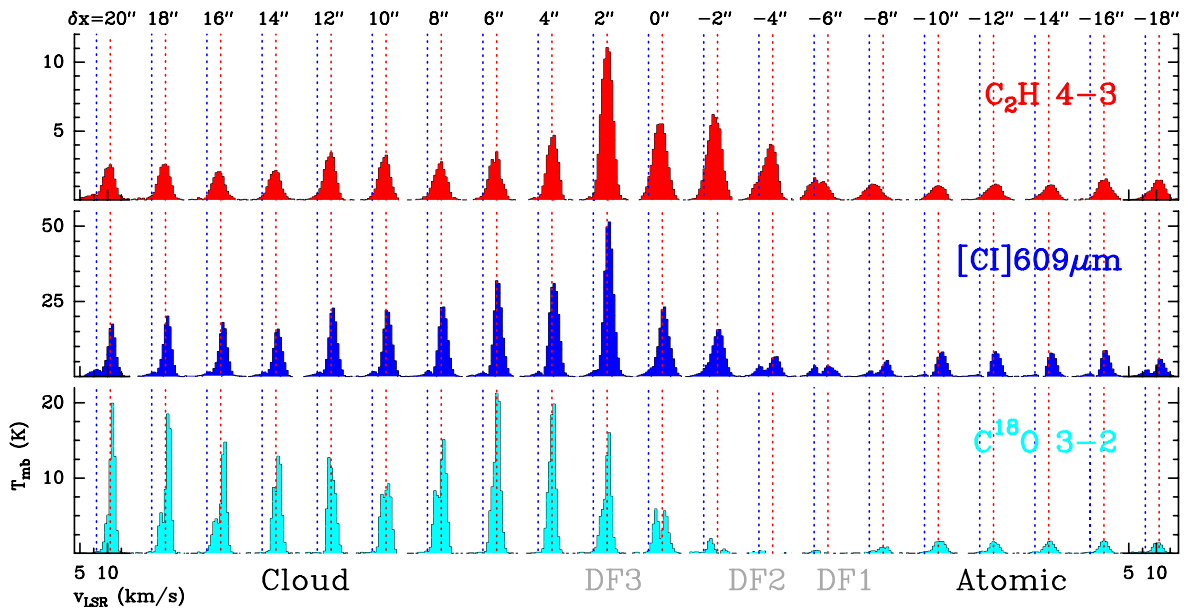


Fig. 5. Spectra along cut A, in the direction of FUV illumination from the Trapezium (from the right). The figure shows spectra averaged over $2'' \times 2''$ boxes. The red dashed lines mark typical velocity centroid of the Bar PDR emission at $v_{\text{LSR}} \approx 10.5 \text{ km s}^{-1}$. The blue dashed lines mark the typical velocity centroid of the background OMC-1 emission at $v_{\text{LSR}} \approx 8 \text{ km s}^{-1}$. This is a minor component of the total line intensity within the PDR.

of the $v_{\text{LSR}} \approx 10\text{--}11 \text{ km s}^{-1}$ component (the PDR) remains approximately constant throughout the Bar (Fig. C.2). C^{18}O shows minimal contribution from the $v_{\text{LSR}} \approx 8 \text{ km s}^{-1}$ component (OMC-1), but most positions exhibit a faint component at $\sim 9.5 \text{ km s}^{-1}$. This suggests either the presence of two sub-components in the Bar or double-peaked profiles caused by slow radial motions. Finally, we detect emission within the atomic PDR at the LSR velocity of the Bar. This emission is more difficult to interpret as molecular abundances in this zone are expected to be negligibly low (Sect. 5).

4. Analysis: Zoom to the DFs

Figure 6 shows a zoom to a small FoV ($\sim 18'' \times 4''$) observed with NIRSpec and MIRI-MRS. Mid-IR MIRI-MRS observations probe the lower-energy H_2 pure-rotational lines. To first order, the intensity of these collisionally-excited $\text{H}_2 v=0\text{--}0$ low- J lines (Fig. 6) is proportional to the column density of warm molecular hydrogen, $N_{\text{warm}}(\text{H}_2)$ (Sect. 4.1 and Van De Putte et al. 2024). The green cross in Fig. 6 marks the $\text{C}_2\text{H } N=4\text{--}3$ emission peak in DF3. This peak nearly coincides with the IR H_2 emission peak.

4.1. $N(\text{H}_2)_{\text{warm}}$ and $T_{\text{rot}}(\text{H}_2)$ across the PDR

Figure 7 displays the vertically-averaged intensity crosscut C extracted along the small FoV observed with JWST spectrometers (Figs. 2c and 6). Pure rotational $\text{H}_2 v=0\text{--}0$ $S(2)$ and $S(4)$ lines at $12.3 \mu\text{m}$ and $8.1 \mu\text{m}$ are the lowest energy *para*- H_2 lines observed by MIRI-MRS. The intensities of these lines are much less affected by foreground extinction than the *ortho*- H_2 $S(3)$ line at $9.6 \mu\text{m}$ (i.e., within the $9.7 \mu\text{m}$ silicate grain absorption feature). Assuming optically thin H_2 line emission and no foreground extinction, one can convert the observed $\text{H}_2 v=0\text{--}0$ $S(4)$ and $S(2)$ line intensities into $J=6$ and $J=4$ level column densities (N_6 and N_4), and derive the rotational temperature T_{64} as:

$$T_{64} = \frac{-\Delta E_{64}/k}{\ln(N_6 g_4 / N_4 g_6)}, \quad (1)$$

where $\Delta E_{64}/k$ is the energy level difference, and g are the level degeneracies. This calculation leads to peak T_{64} values of $\sim 600 \text{ K}$

in DF2 and DF3 (see also Van De Putte et al. 2024, Sidhu in prep.). Figure C.5 shows the resulting T_{64} profile across cut C. Interestingly, $I(\text{C}_2\text{H } 4\text{--}3)$ does not follow the T_{64} profile (see Fig. C.5). Instead, it more closely follows the H_2 emission and is well correlated with the FUV-pumped H_2 emission (Appendix D).

The $S(2)$ and $S(4)$ lines have relatively low critical densities (n_{cr}) for $\text{H}_2\text{--H}_2$ inelastic collisions (from a few 10^3 to several 10^5 cm^{-3} at $T \approx 600 \text{ K}$; Wan et al. 2018; Hernández et al. 2021). This n_{cr} is comparable or lower than the gas density in the DFs (Peeters et al. 2024). Thus, T_{64} is a good proxy of the gas temperature in the IR H_2 -emitting gas (only if $n_{\text{H}_2} \ll n_{\text{cr}}$, then $T_{64} \ll T_k$).

We also estimated the column density of warm H_2 along each line of sight in crosscut C. Assuming a Boltzmann population of the N_4 and N_6 levels at T_{64} , we determine $N_{\text{warm}}(p\text{-H}_2)_{\text{LTE}}$ as:

$$N_{\text{warm}}(p\text{-H}_2)_{\text{LTE}} = \frac{N_4}{g_4} Q(T_{64}) e^{+E_4/kT_{64}}, \quad (2)$$

where $Q(T)$ is the rotational partition function of $p\text{-H}_2$. The total column density of warm H_2 , $N_{\text{warm}}(\text{H}_2)_{\text{LTE}}$, is equal to $N_{\text{warm}}(p\text{-H}_2)_{\text{LTE}} (1 + \text{OTP})$, where OTP is the H_2 ortho-to-para ratio. The H_2 OTP ratio across the Bar is fairly constant and equal to three (Van De Putte et al. 2024, Sidhu in prep.).

Figure 7 shows the resulting $N_{\text{warm}}(\text{H}_2)_{\text{LTE}}$ profile (dashed magenta curve) across cut C. This curve peaks at DF3, DF2, and DF1, roughly following the low-energy $\text{H}_2 v=0\text{--}0$ $S(1)$ emission profile. In reality, foreground and internal extinction in the PDR dim the IR H_2 line emission. Although this attenuation is not large toward Orion, in particular toward the edge of the cloud, we included a line intensity extinction correction as $I_{\text{corr}} = I_{\text{obs}} e^{+\tau_\lambda}$, with $\tau_\lambda = A_\lambda/1.086$ and $A_\lambda/A_V = 0.045$ at the wavelength of the $S(2)$ and $S(4)$ lines (appropriate to Orion; Declair et al. 2022; Gordon et al. 2023). Table 3 provides the corrected $N(\text{H}_2)_{\text{warm}}$ values toward DF3, DF2, and DF1 using two extinction estimations: those of Peeters et al. (2024) and Van De Putte et al. (2024). These calculations yield a reasonable range of total column densities in these DFs, assuming $N_{\text{H}} \approx N(\text{H}) + 2 N(\text{H}_2)_{\text{warm}}$ and $N(\text{H}) \approx N(\text{H}_2)_{\text{warm}}$. We obtain N_{H} values of $2.61\text{--}4.73$, $2.33\text{--}3.33$, and $4.92\text{--}2.75$ times 10^{21} cm^{-2} in DF3, DF2, and DF1, respectively for the two extinction corrections mentioned above.

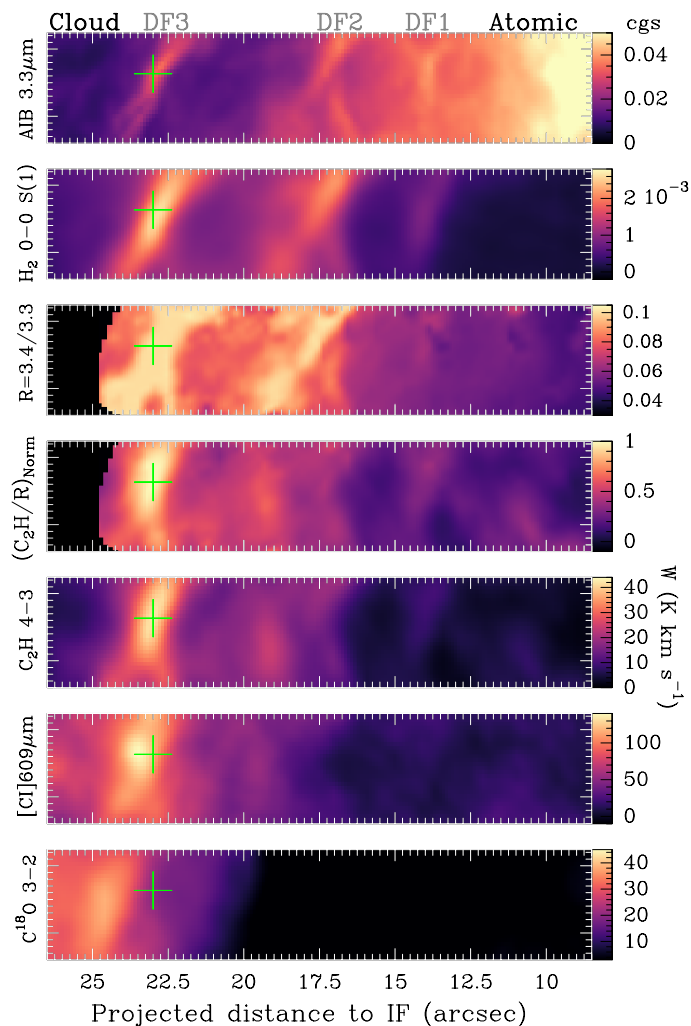


Fig. 6. Small FoV observed with NIRSpc and MIRI-MRS spectrometers. The green cross shows a $C_2H\ N=4-3$ emission peak in DF3 region. This peak nearly coincides with the IR H_2 emission peak. “cgs” refers to $\text{erg s}^{-1} \text{cm}^{-2} \text{sr}^{-1}$. The $(C_2H/R)_{\text{Norm}}$ map refers to the normalized $C_2H\ N=4-3$ line intensity divided by the normalized $3.4/3.3\ \mu\text{m}$ AIB ratio. Figure 7 shows vertically averaged intensity cuts of this field.

4.2. Geometry and origin of the small-scale H_2 DFs

Adopting a typical gas density, n_H , of a few $10^5\ \text{cm}^{-3}$ in the DFs, based on an analysis of the mid-IR H_2 emission (Van De Putte et al. 2024) and consistent with Sect. 4.4—which assumes that the $C_2H\ 4-3$ and H_2 rotational emissions are nearly co-spatial⁴—the inferred N_H columns imply a scale size along the line of sight (l-o-s) of $l_{\text{los}} = N_H/n_H \approx 10^{16}\ \text{cm}$ ($\sim 0.003\ \text{pc}$). As DF1 and DF2 show either no or very faint $C^{18}O$ emission, they are translucent to FUV radiation, indicating extinction depths in the plane of the sky (δx ; the FUV illumination direction) of $\Delta A_V \lesssim 1\ \text{mag}$, or $N_{H,\delta x}$ of a few $10^{21}\ \text{cm}^{-2}$, which gives $l_{\delta x} \lesssim 10^{16}\ \text{cm}$. These δx and l-o-s spatial scale sizes ($\sim 1''-2''$, in agreement with the observed emission width in δx) are smaller than the size of the elongated H_2 -emitting structure in the δy direction. Therefore, one possibility is that DF1 and DF2 are true small-scale filaments, whose lengths are significantly greater than their widths. Since they run roughly parallel to the IF, they may represent the effects of a shockwave

⁴ As observed (e.g., Fig. 7) and predicted by our PDR model (Fig. 10).

propagating into the molecular cloud, driven by FUV radiation (e.g., Hill & Hollenbach 1978; Bron et al. 2018) and perhaps by stellar winds from $\theta^1\ \text{Ori C}$ (Pabst et al. 2019, 2020). This shockwave would lead to localized gas compression and minor density perturbations (see also Goicoechea et al. 2016). Another possibility is that these DFs represent a terraced-field-like cloud structure (i.e., multiple cloud surfaces; Habart et al. 2024; Peeters et al. 2024), with several steps seen from above, to account for the succession of nearly edge-on DFs. The lack of significant $C^{18}O$ emission in DF1 and DF2, however, would imply that gas densities are much lower than in DF3 and DF4. Hydrodynamical simulations will be needed to confirm these two scenarios (filaments and sheets vs. cloud surfaces) as well as their origin.

DF3 and other H_2 -emitting structures that border the molecular cloud traced by bright $C^{18}O\ 3-2$ emission (Fig. C.3) correspond to FUV-illuminated rims of larger, likely denser molecular gas structures or clumps (Lis & Schilke 2003). In DF3, l_{los} (warm H_2) is also $\sim 10^{16}\ \text{cm}$, which is significantly smaller than the projected size of the $C^{18}O$ -emitting structure (several arcseconds). This suggests that the IR H_2 emission traces only the limb of roughly spherical structures, which may be remnants of cloud turbulence (e.g., Hartmann & Burkert 2007; Glover & Mac Low 2011; Federrath & Klessen 2013) or produced by photoevaporation processes (e.g., Gorti & Hollenbach 2002).

4.3. C_2H emission and the $3.4/3.3\ \mu\text{m}$ AIB ratio

The C_2H emission approximately follows local enhancements of the $3.3\ \mu\text{m}$ AIB intensity, which is proportional to the abundance of the carriers, to the total column density N_H , and to the local flux of FUV photons (e.g., Habart et al. 2024). Interestingly, the spatial distribution of the C_2H emission more closely resembles the observed peaks of the $3.4/3.3\ \mu\text{m}$ AIB intensity ratio (Figs. 6 and 7). The $3.4\ \mu\text{m}$ AIB emission is generally assigned to C–H stretching mode of a small quantity of H atoms bonded to sp^3 C atoms, either in hydrocarbon radical groups (mostly $-CH_3$, so-called methylated-PAHs e.g., Jourdain de Muizon et al. 1990; Joblin et al. 1996) or super-hydrogenated PAHs (Schutte et al. 1993; Bernstein et al. 1996). The latter are not really expected to dominate in the Bar, as any extra H atom will be quickly photo-detached (when $G_0/n(H) > 0.03$; Andrews et al. 2016). Other studies associate the $3.4/3.3\ \mu\text{m}$ AIB ratio to the hydrogenation levels of carbonaceous “nanograins” (Elyajouri et al. 2024). Regardless of the nomenclature, the carriers are in the molecular domain and must be highly excited to emit at $3.4\ \mu\text{m}$. Here, we attribute the $3.4/3.3\ \mu\text{m}$ AIB ratio to the aliphatic-to-aromatic content of PAHs in the Bar (e.g., Joblin et al. 1996; Pilleri et al. 2015; Li & Draine 2012; Yang et al. 2016; Peeters et al. 2024; Schroetter et al. 2024). This is also supported by the presence of weak bands at $\sim 6.9\ \mu\text{m}$ in DF3 and DF2, likely originating from CH deformation modes of aliphatic groups (Chown et al. 2024).

The aliphatic C–H bonds are easier to dissociate than the aromatic C–H bonds in the PAH skeleton (Marciniak et al. 2021). Indeed, the $3.4/3.3\ \mu\text{m}$ AIB intensity ratio is remarkably low (~ 0.04) in the atomic PDR (Peeters et al. 2024; Chown et al. 2024; Schroetter et al. 2024; Pasquini et al. 2024), which is exposed to a stronger FUV field (higher flux and photon energy) than the DFs. The $3.4/3.3\ \mu\text{m}$ AIB ratio increases up to ~ 0.1 in DF3 (still modest compared to PDRs of lower G_0 ; e.g., Joblin et al. 1996; Mori et al. 2014), where it coincides with the maximum value of $I(C_2H\ 4-3)$. In general, the $3.4/3.3\ \mu\text{m}$ AIB ratio follows the C_2H emission profile (see also Fig. D.2), where local peaks of the ratio coincide with local peaks of $I(C_2H\ 4-3)$. This implies that the conditions triggering the formation of simple

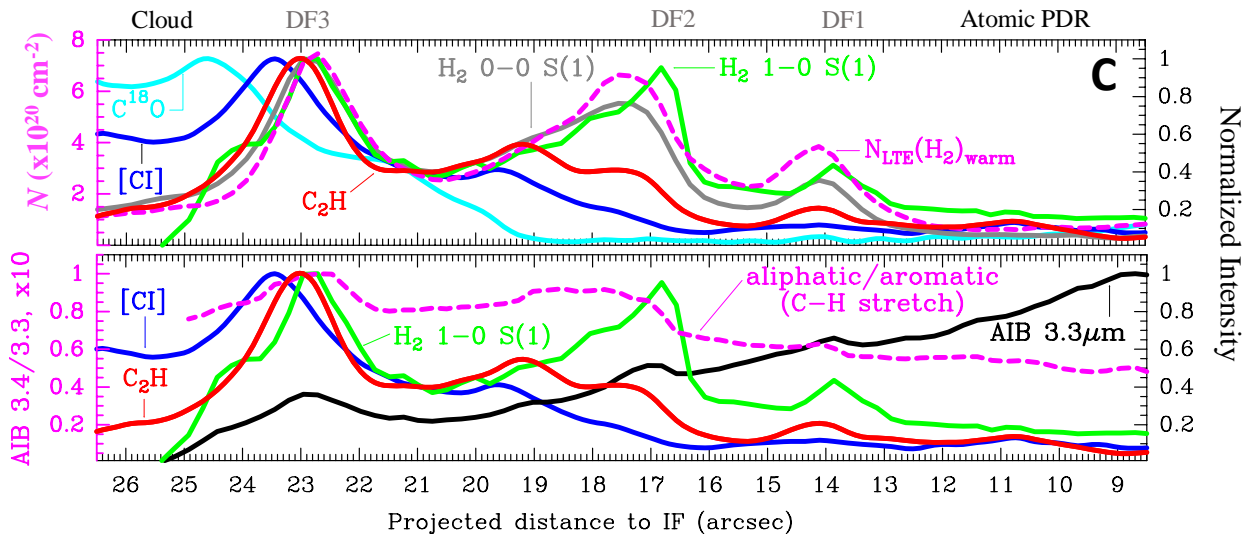


Fig. 7. Vertically-averaged crosscut C, with $\Delta(\delta y) = 2''$. This cut passes through the green cross in Fig. 6. *Upper panel:* The magenta dashed curve shows the column density of warm H_2 obtained from $v=0-0$ $S(4)$ and $S(2)$ lines, observed with MIRI-MRS, assuming a Boltzmann distribution at $T_{64} (\approx 600$ K, shown in Fig. C.5). *Bottom panel:* The magenta dashed curve shows the 3.4/3.3 μm AIB intensity ratio ($\times 10$) from NIRSspec.

Table 1. Warm H_2 and total column densities in selected dissociation front positions of the Orion Bar PDR.

Position	$N(H_2)_{\text{warm}}$	$N_{\text{H}}^{(a)}$	$N(H_2)_{\text{warm}}$	$N_{\text{H}}^{(a)}$	$N(H_2)_{\text{warm}}$	$N_{\text{H}}^{(a)}$
	[cm^{-2}]	[cm^{-2}]	[cm^{-2}]	[cm^{-2}]	[cm^{-2}]	[cm^{-2}]
	No extinction correction		Correction 1 ^(b)		Correction 2 ^(c)	
DF1	3.50×10^{20}	1.05×10^{21}	1.64×10^{21}	4.92×10^{21}	9.07×10^{20}	2.72×10^{21}
DF2	5.42×10^{20}	1.63×10^{21}	7.76×10^{20}	2.33×10^{21}	1.11×10^{21}	3.33×10^{21}
DF3	7.47×10^{20}	2.24×10^{21}	8.71×10^{20}	2.61×10^{21}	1.58×10^{21}	4.73×10^{21}

Notes. ^(a)Total column density with respect to H nuclei assuming $N_{\text{H}} \approx N(\text{H}) + 2N(H_2)_{\text{warm}}$ and $N(\text{H}) \approx N(H_2)_{\text{warm}}$ in these DFs. ^(b)Extinction determined in the intermingled formalism by Peeters et al. (2024). The total (foreground and internal) visual extinction toward DF1, DF2 and DF3 positions is 37.3, 8.64, and 3.70 mag, respectively (see their Table 1). ^(c)Extinction determined by Van De Putte et al. (2024) assuming a screen geometry and 23, 14, and 18 mag of visual extinction toward DF1, DF2, and DF3, respectively.

hydrocarbons also favor the formation (and survival) of PAHs with aliphatic side groups. Furthermore, the enhanced abundances of related small hydrocarbon radicals at these peaks may also indicate a causal relationship⁵ between these radicals and the aliphatic content of PAHs (see Sect. 6.3).

4.4. C_2H abundance, n_{H} , and T at the radical peaks

Here we investigate the range of gas density, temperature, and C_2H column density that reproduces the peak $I(C_2H N = 4-3)$ line intensities in the main DFs. To do so, we updated our nonlocal non-LTE radiative transfer Monte Carlo model (Goicoechea et al. 2022) to treat the rotational excitation of C_2H by inelastic collisions with $o\text{-}H_2(J=1)$, $p\text{-}H_2(J=0)$, and e^- (for details, see Appendix E). We set the molecular gas fraction, $f(H_2) = 2n(H_2)/n_{\text{H}}$, to 2/3, with $n_{\text{H}} = n(\text{H}) + 2n(H_2)$. This choice implies $n(H_2) = n(\text{H})$, which is appropriate for a DF. We also include radiative excitation by dust continuum pho-

⁵ Figure 6 shows the normalized $C_2H 4-3$ line intensity divided by the normalized 3.4/3.3 μm AIB ratio. This quantity peaks in DF3. The 3.4/3.3 μm ratio globally decreases from the DFs to the atomic PDR (due to the photoerosion of aliphatic side groups; Peeters et al. 2024; Chown et al. 2024), but it declines less steeply than $I(C_2H 4-3)$. Thus, this quantity remains < 1 and decreases from DF3 to the atomic PDR.

tons (Appendix E) consistent with the far-IR and submm continuum detected in the Bar (Arab et al. 2012; Salgado et al. 2016). Figure 8 shows a grid of single-component models⁶ where we plot $I(C_2H 4-3 J = 9/2-7/2)$ as a function of n_{H} for different gas temperatures. Taking $T_{\text{k}} = 600$ K as an upper limit, the observed $I(C_2H 4-3)$ line intensities in DF3 and DF4 can be reproduced with $N(C_2H) \lesssim 10^{15} \text{ cm}^{-2}$ and n_{H} of a few 10^5 cm^{-3} . The best model of DF2 implies $N(C_2H) \approx 5 \times 10^{14} \text{ cm}^{-2}$. The inferred C_2H column densities make C_2H the most ubiquitous of all polar hydrocarbons detected by Cuadrado et al. (2015) in the Bar. We determine the peak C_2H abundance ($[C_2H] = N(C_2H)/N_{\text{H}}$) using the N_{H} column densities in Table 1. This leads to $[C_2H] \approx (2-4) \times 10^{-7}$ in DF3 and $[C_2H] \approx 2 \times 10^{-7}$ in DF2. These values are significantly higher than the abundances previously inferred from low-resolution observations of PDRs, which dilute the emission from small spatial-scale DFs (e.g., Fuente et al. 1996; van der Wiel et al. 2009; Nagy et al. 2015).

⁶ We run single-component models (single T_{k} and n_{H}), but the model discretizes the emission zone into multiple slabs to account for the nonlocal character of molecular excitation and line photon transport. We include thermal, opacity, and turbulent line broadening, with $\sigma_{\text{turb}} = 1 \text{ km s}^{-1}$ (matching the observed line-widths). These models predict a rotational temperature of $T_{\text{rot}}(C_2H 4-3) = 20-24$ K, which is much lower than T_{k} due to non-LTE subthermal excitation, in agreement with the excitation temperature inferred from a rotational diagram (Fig. F.1).

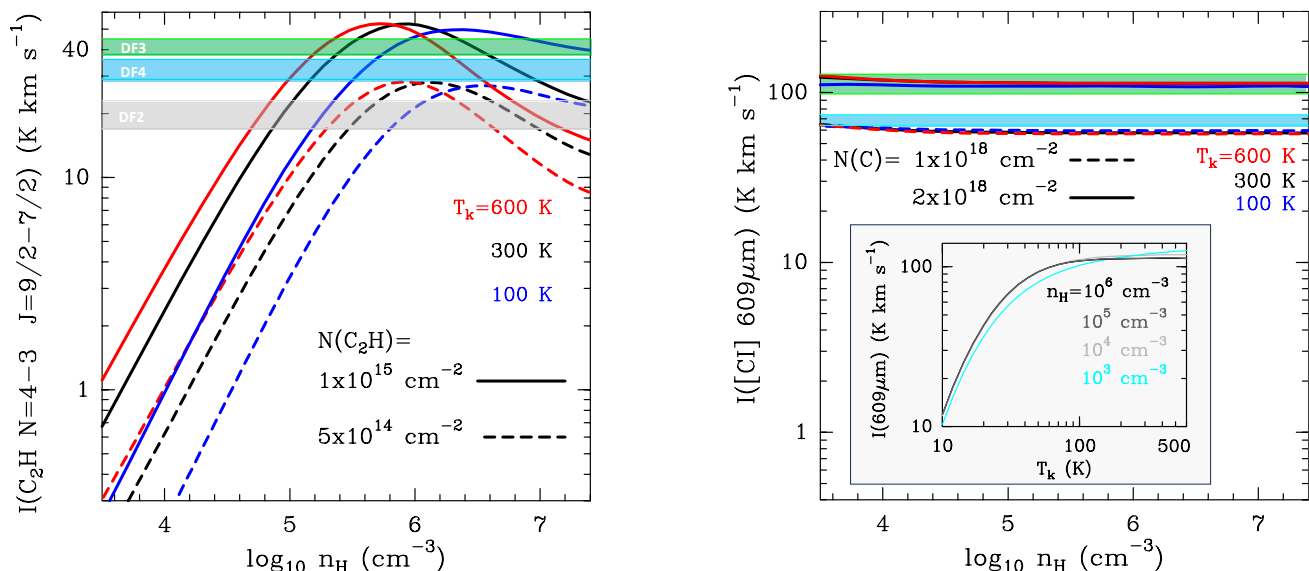


Fig. 8. Results from nonlocal and non-LTE radiative transfer models of C_2H (left) and $[C I]$ (right) for different values of T_k and n_H (single-component models⁶). The horizontal green, blue, and grey shaded areas show the observed peak intensities and 1σ dispersions.

4.5. Atomic carbon at the $[C I]$ 609 μm peaks

The $[C I]$ 609 μm line involves a forbidden transition with a very low Einstein coefficient for spontaneous emission. In the molecular PDR, inelastic collisions of $C(^3P)$ atoms with H_2 dominate the excitation of the $[C I]$ fine-structure lines. Since high-temperature, >100 K, $C(^3P)$ - o/p - H_2 inelastic collisional rates did not exist in the literature, we extended the scattering calculations of Kłos et al. (2018, 2019) to 3000 K (see Appendix H). The right panel of Fig. 8 shows a grid of $[C I]$ models. Because of the resulting low excitation requirement of the $[C I]$ 609 μm line—low critical density ($\approx 10^3$ cm^{-3}) and low level energy separation compared to T_k close to the DFs ($\Delta E/k_b = 23.6$ K $\ll T_k$)—the $[C I]$ 609 μm emission is optically thin, collisionally excited, and nearly thermalized ($T_{ex} \approx T_k$). In this regime ($T_k > 100$ K and $n(H_2) > 10^4$ cm^{-3}), $I([C I] 609 \mu m)$ is proportional to $N(C)$ quite irrespective of the physical conditions (inset in Fig. 8 right). We obtain $N(C) \approx 2 \times 10^{18}$ cm^{-2} and $\lesssim 10^{18}$ cm^{-2} at the $I([C I])$ peaks, slightly behind DF3 and DF4, respectively. Assuming that atomic carbon becomes the major gas-phase reservoir of carbon at the $I([C I])$ peak (with $[C/H] = 1.4 \times 10^{-4}$; Fig. 9), these $N(C)$ values imply that N_H increases from several 10^{21} cm^{-2} at the H_2 emission peak in DF3, to $N_H \approx N(C)/[C/H] \approx 10^{22}$ cm^{-2} at the $I([C I])$ peak, slightly behind. This increase in N_H is consistent with $[C I]$ tracing slightly deeper layers of the molecular structure or clumps associated to $C^{18}O$, and suggests a density gradient.

5. PDR models of the main dissociation fronts

To understand the origin of the high C_2H abundances in the Orion Bar, we model the hydrocarbon radical chemistry using version 1.7 of the Meudon PDR code (Le Petit et al. 2006). We updated the chemical network with the reaction rates we implemented to model the chemistry of CH_3^+ in d203-506 (Berné et al. 2023), including the newly computed photodissociation cross-section for CH_3^+ (Mazo-Sevillano et al. 2024). Our gas-phase chemical network includes v -state-dependent rate constants for reaction of FUV-pumped ro-vibrationally excited H_2 (hereafter H_2^*) with C^+ , O, S^+ , S, and N (e.g., Zanchet et al. 2019; Veselinova et al. 2021; Goicoechea & Roncero 2022). These nonthermal reactions play a key role in initiating the gas chemistry in dense PDRs

(e.g., Sternberg & Dalgarno 1995). We also include simple gas-grain exchanges for O, OH, H_2O , O_2 , C, and CO. These species adsorb on dust grains as temperatures drop, are photo-desorbed by FUV photons, desorb via cosmic-ray impacts, and thermally sublimate. Only for water ice formation, we include the grain surface reactions $s-O + s-H \rightarrow s-OH$ and $s-OH + s-H \rightarrow s-H_2O$ (e.g., Hollenbach et al. 2009; Putaud et al. 2019), where s - refers to the species in the solid. Our model does not include PAH chemistry.

Following our previous studies (e.g., Cuadrado et al. 2015; Bron et al. 2018; Joblin et al. 2018), we generically model the molecular DFs as constant thermal-pressure structures (i.e., with gas density gradients). Table 2 summarizes the main input parameters. In the Bar, G_0 is $\sim 6 \times 10^4$ at the IF (median value of Peeters et al. 2024). The exact FUV flux reaching each DF depends on their three-dimensional structure and location with respect to the incoming FUV radiation, as well as on the properties of the atomic PDR. Since the $I(3.3 \mu m$ AIB) emission is approximately three times lower in DF3 than in the IF (Fig. 3), we adopt a reference model with a representative value of $G_0 = 2 \times 10^4$, but the main results do not depend on the exact value. The upper panel in Fig. 9 shows the resulting physical structure for a reference model with a constant thermal pressure $P_{th}/k_B = n_H T_k = 10^8$ K cm^{-3} , which

Table 2. Main parameters used in the PDR models of the main DFs.

Model parameter	Value	Note
FUV illumination, G_0	2×10^4 Habing	
A_V (depth into the PDR)	10 mag	
Thermal pressure P_{th}/k	$(0.2-2) \times 10^8$ cm^{-3} K	Isobaric
Density $n_H = n(H) + 2n(H_2)$	$n_H = P_{th} / kT_k$	Gradient
$R_V = A_V/E_{B-V}$	5.5	Orion ^a
Cosmic Ray ζ_{CR}	10^{-16} H_2 s^{-1}	
Abundance O/H	2.6×10^{-4}	Orion ^b
Abundance C/H	1.4×10^{-4}	Orion ^b
Abundance S/H	1.4×10^{-5}	Orion Bar ^c

Notes. ^aCardelli et al. (1989). ^bSofia et al. (2004). ^cGoicoechea & Cuadrado (2021) and Fuente et al. (2024).

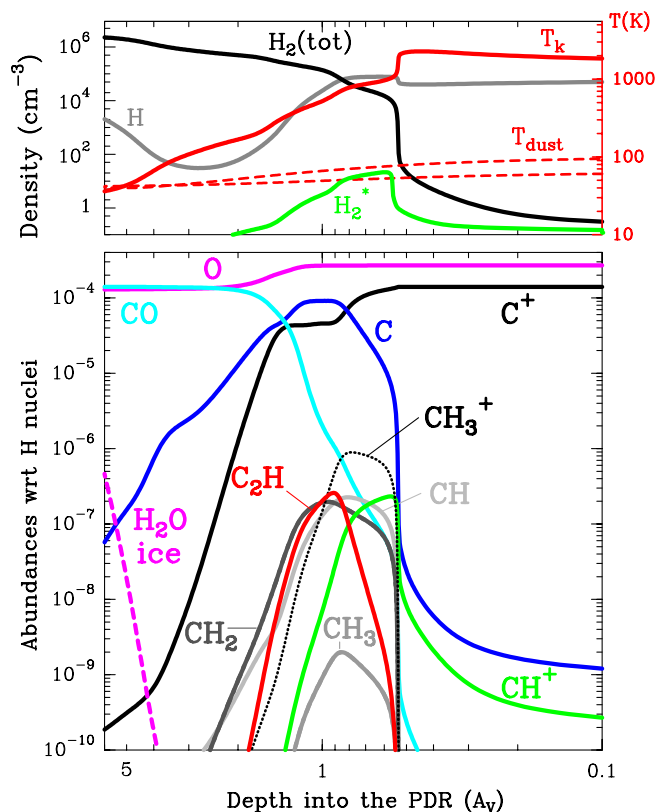


Fig. 9. Isobaric PDR model with $G_0 = 2 \times 10^4$ and $P_{\text{th}}/k = 10^8 \text{ K cm}^{-3}$. *Upper panel:* Gas density, gas temperature (T_k), and grain-size distribution maximum and minimum dust temperature (T_{dust}) profiles as a function of A_V depth into the PDR. The green curve shows the density of FUV-pumped H_2^* ($v \geq 1$). *Lower panel:* Abundance profiles with respect to H nuclei for the main species discussed in the text.

provides the best fit to the complete set of (beam-dilution corrected) $\text{C}_2\text{H } N = 1-0$ to $10-9$ line intensities (see Appendix G).

In these generic models, the low- $A_V \approx 0.1$ mag layers represent the atomic PDR, or the inter-filament environment, with $n_{\text{H}} \approx 5 \times 10^4 \text{ cm}^{-3}$. The $A_V \lesssim 1$ mag zone is more representative of DF2, whereas $A_V \geq 1$ mag represents DF3. The green curve shows the density profile of FUV-pumped H_2^* ($v \geq 1$), which traces the steep rise in H_2 abundance upon entering the DF. The lower panel shows the abundance profiles of gas-phase CO, C, and C⁺, along with those of C_2H , CH⁺, CH₃⁺, and related radicals (CH, CH₂, and CH₃). In agreement with our C_2H observations, the predicted abundance of these radicals reaches a maximum at the DF, where $n(\text{H}) \approx n(\text{H}_2)$. Hence, our term ‘hydrocarbon radical peak’. The dashed curve shows the water-ice abundance profile. Given the high G_0 , dust temperatures and photodesorption rates are large enough to prevent the formation of abundant water ice in the PDR, which would otherwise deplete the volatile oxygen. Therefore, the gas in the DFs is oxygen-rich, meaning $[\text{C}]/[\text{O}] \approx 0.5$.

The model predicts steep temperature and density gradients at small spatial scales, ranging from $T_k \approx 700-600 \text{ K}$ and n_{H} of a few 10^5 cm^{-3} at the hydrocarbon radical peak, to $T_k \approx 150 \text{ K}$ and $n_{\text{H}} \gtrsim 10^6 \text{ cm}^{-3}$ at the CO-rich zone. Figure 10 shows that the predicted angular separation between the local emissivities of $\text{H}_2 0-0 S(1)$, $\text{C}_2\text{H } N = 4-3$, and $[\text{C I}] 609 \mu\text{m}$ lines is very small, less than $1''$ (for an edge-on PDR). This model predicts that the CO/C and H_2/H transition zones are separated by 0.0015 pc , which agrees with the observed emission stratification in DF3 (Fig. 3). If $P_{\text{th}}/k_{\text{B}}$ increases (decreases) by a factor of two, the predicted separation decreases (increases) by a factor of three.

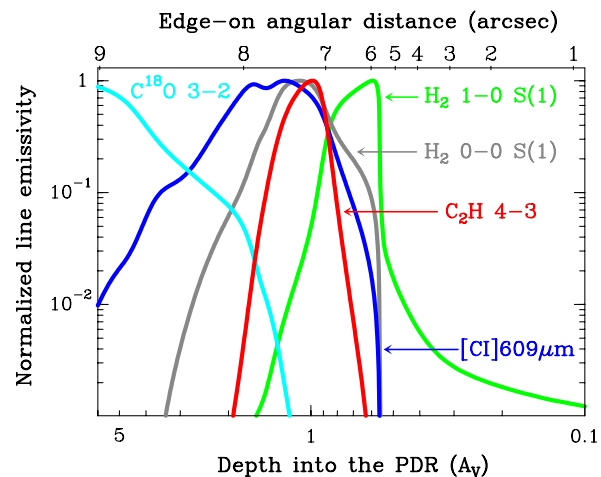
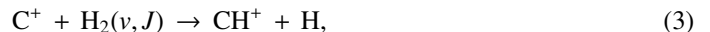


Fig. 10. Local line emissivities predicted by a PDR model with $P_{\text{th}}/k_{\text{B}} = 10^8 \text{ K cm}^{-3}$. The upper horizontal axis shows the equivalent angular scale for a perfectly edge-on PDR. These distances will decrease as the inclination of the PDR with respect to a edge-on PDR increases.

6. Discussion

6.1. FUV-driven gas-phase hydrocarbon chemistry

Figure 11 summarizes the dominant gas-phase reactions of simple hydrocarbons in our reference model. The starting reaction is:



which has an endoergicity⁷ of $\Delta E/k = 4,300 \text{ K}$ when H_2 is in the ground state (Hierl et al. 1997; Zanchet et al. 2013). Thus, this reaction is exceedingly slow and inefficient in cold clouds shielded from FUV radiation. The warm temperatures and enhanced abundances of FUV-pumped H_2^* ($v \geq 1$) in dense PDRs (detected up to $v = 12$ in the Bar, Kaplan et al. 2021) overcomes the reaction endoergicity. This triggers the formation of abundant CH^+ (e.g., Agúndez et al. 2010), which peaks slightly ahead of the DF, where H_2^* ($v \geq 1$) reaches its highest abundance. CH^+ ro-vibrational line emission is readily detected along the Bar (Naylor et al. 2010; Nagy et al. 2013; Parikka et al. 2017; Zannese et al. 2025). Subsequent (fast) exothermic hydrogenation reactions lead to the formation of CH_3^+ (the methyl cation, first detected in space by JWST in the irradiated disk d203-506 (Berné et al. 2023) and also present in the Bar (Zannese et al. 2025)). CH_3^+ reacts extremely slowly with H_2 due its very high endothermicity (and no CH_4^+ products are observed in experiments; Smith et al. 1982; Asvany et al. 2004) and is predicted to be the most abundant hydrocarbon in the DF (Fig. 9). CH_3^+ destruction is dominated by dissociative recombination, leading to the formation of abundant radicals CH_2 (methylene) and CH (methylidyne). The slower CH_3^+ radiative association leads to somewhat lower levels of CH_3 (methyl).

In PDRs, hydrogen abstraction reactions play a key role in the gas-phase growth of simple hydrocarbons. In Fig. 11, however, the reactions indicated by red arrows are endoergic. Thus, they are very slow in cold gas but, similarly to reaction (3), become fast in FUV-irradiated gas due to the high temperatures and presence of FUV-pumped H_2^* . These reactions boost the formation of CH, CH₂, and CH₃ radicals. These radicals further react with C⁺, promoting the formation of hydrocarbons with two carbon atoms. CH is abundant in the Bar (and correlates with the C_2H emission, Nagy et al. 2017) and across large scales in OMC-1 (Goicoechea et al. 2019), following the spatial distribution of

⁷ Reaction 3 becomes exoergic for H_2^* at $v = 0$, $J \geq 11$, and $v = 1$, $J \geq 7$.

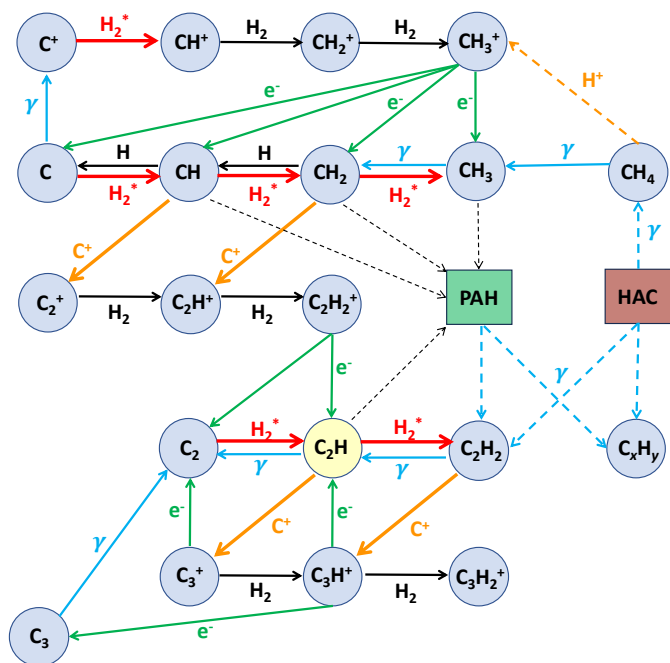


Fig. 11. Dominant gas-phase formation and destruction pathways at the hydrocarbon radical peak (model in Fig. 9). Red arrows show endoergic reactions. These reactions become fast at high T or where significant FUV-pumped H_2^* exists. We also show possible reactions (dashed) involving PAHs and HAC grains, which may be relevant in certain conditions.

CH^+ and $[\text{C II}]$ 158 μm (Goicoechea et al. 2019). This suggests that reactions of CH and C^+ drive the formation of C_2^+ , which starts the gas-phase formation of hydrocarbons with two C atoms.

The enhanced abundances of CH_n^+ cations and CH_n radicals are a key feature of the carbon chemistry in FUV-irradiated gas. As observed in the Bar, their peak abundances occur ahead of the CO/C transition, implying that C^+ and H_2^* are abundant. The abundances of simple hydrocarbons increase with rising P_{th} due to corresponding increase in gas temperature, density, and H_2^* ($v \geq 1$) abundances. The C_2H abundance reaches a maximum at the DF (slightly behind the CH^+ peak). At this maximum, C_2H formation is dominated by reaction:



which has an energy barrier⁸ of $\Delta E/k = 1500$ K (Pitts et al. 1982). On the other hand, destruction of C_2H is dominated by photodissociation, reactions with H_2 , and reactions with C^+ . The reference model with $P_{\text{th}}/k_B = 10^8$ K cm^{-3} predicts a peak $[\text{C}_2\text{H}]$ abundance of $\approx 2.5 \times 10^{-7}$, which agrees with the abundance derived from observations of DF3 and DF2 (Sect. 4.4). The predicted $N(\text{C})/N(\text{C}_2\text{H})$ column density⁹ ratio across the PDR, $\sim 10^3$, also matches the observed value (Sect. 4.5). Lower P_{th} values underestimate the C_2H abundances and line intensities (Appendix G).

⁸ Since state-dependent rate constants, $k_{v,J}(T)$, do not exist for reactions $\text{H}_2(v, J) + \text{CH}_n \rightarrow \text{CH}_{n+1} + \text{H}$ and for reaction 4, we modeled them by adopting state-dependent rate constants where the energy $E_{v,J}$ of each H_2^* ro-vibrational state is subtracted from the reaction endoergicity ΔE (when $\Delta E > E_{v,J}$). That is, $k_{v,J}(T) \propto \exp(-[\Delta E - E_{v,J}]/k_B T)$. Thus, we assume that all internal energy of H_2^* is used to overcome the barrier.

⁹ The (face-on PDR) column densities predicted by this model are $N(\text{C}) = 2 \times 10^{17} \text{ cm}^{-2}$ and $N(\text{C}_2\text{H}) = 2 \times 10^{14} \text{ cm}^{-2}$, a factor of ~ 10 lower than the observed values (Sects. 4.4 and 4.5). This implies a geometrical intensity enhancement ($\sin \alpha$)⁻¹ ≈ 10 , corresponding to a PDR tilt angle of $\alpha \approx 5^\circ$, as commonly found for the Bar (e.g., Peeters et al. 2024).

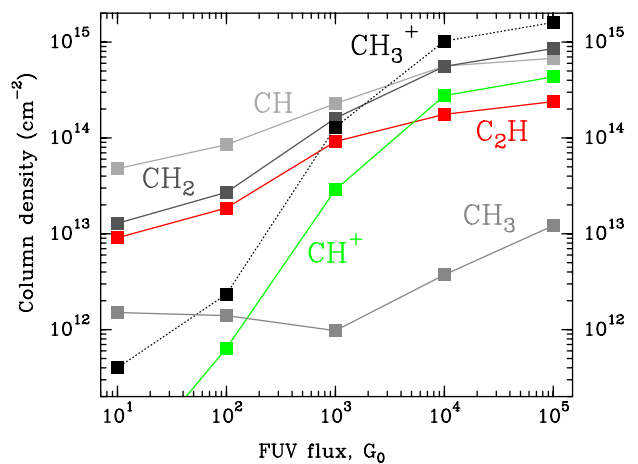


Fig. 12. Predicted column densities of simple hydrocarbon radicals, CH^+ , and CH_3^+ as a function of increasing G_0 . These models refer to a face-on PDR with $A_{V,\text{tot}} = 10$ mag, and a constant density of $n_{\text{H}} = 10^5 \text{ cm}^{-3}$.

Our observations and models demonstrate how FUV radiation triggers a specific gas-phase hydrocarbon chemistry in dense PDR gas. As G_0 increases, so does the gas temperature and the column density of C^+ and H_2^* . Reaction 3 initiates this chemistry and represents the most relevant destruction mechanism for C^+ at the DFs. This leads to the formation of CO and HCO^+ close to the DFs (as observed by ALMA; Goicoechea et al. 2016). Furthermore, the observed extended spatial distribution of CH^+ $J = 1-0$ and CH rotational emission in OMC-1 (Goicoechea et al. 2019) probes the widespread occurrence of hydrocarbon radical peaks across the irradiated surfaces of OMC-1, including the Bar.

To isolate the role of G_0 on this chemistry, Fig. 12 shows the predicted column densities of simple hydrocarbons as a function of G_0 for a PDR of constant density, $n_{\text{H}} = 10^5 \text{ cm}^{-3}$, representative of n_{H} in the illuminated surfaces of OMC-1 (e.g., Pabst et al. 2024). Fig. 12 shows that $N(\text{CH}^+)$ increases by more than 3 orders of magnitude from $G_0 = 10$ to 10^5 (see also, Agúndez et al. 2010). This enhancement triggers the formation of related hydrocarbons when $G_0 > 10^2$. In these models, CH , CH_2 , CH_3 , and C_2H increase their column densities by factors of ~ 15 , ~ 65 , ~ 10 , and ~ 25 , respectively, compared to low FUV conditions.

Interestingly, the very high C_2H abundances inferred toward the molecular edge of the Bar are similar to those derived in galaxies undergoing vigorous star formation, where the origin of C_2H has been also attributed to gas with very low visual extinction ($A_V < 2$ mag) in the form of thin, irradiated cloud interfaces (García-Burillo et al. 2017). In this context, the enhanced abundances of C_2H serve as a powerful tracer of radiative feedback.

6.2. Are PAH and very small grain photodestruction sources of hydrocarbons in the atomic PDR?

Our observations show faint C_2H emission¹⁰ toward the atomic PDR (Sect. 3.2). However, the gas-phase chemistry described in the previous section results in negligible levels of hydrocarbon radicals within these layers, which are characterized by low A_V and $[\text{H}_2] \ll [\text{H}]$ (see Fig. 9). Therefore, if this emission originates from the Bar (as suggested by its velocity centroid), not

¹⁰ The brightest C_2H features in the atomic PDR zone (and with a line centroid at $v_{\text{LSR}} \approx 10-11 \text{ km s}^{-1}$) show $I(\text{C}_2\text{H } 4-3) \approx 5 \text{ K km s}^{-1}$, which translates into $[\text{C}_2\text{H}] \lesssim 10^{-8}$ (after non-LTE modeling and adopting $n_{\text{H}} \approx (5-10) \times 10^4 \text{ cm}^{-3}$ and $T_k \approx 600-1000 \text{ K}$). These values would represent the maximum C_2H abundance produced by top-down processes.

from background OMC-1 layers, top-down formation processes must be considered; for example photo-processing of PAH, of carbonaceous grains, or both.

Only the most resistant and stable population of PAHs with ≥ 50 C atoms (Bakes et al. 2001; Allain et al. 1996; Andrews et al. 2015; Montillaud et al. 2013) are expected to survive under strong FUV irradiation conditions in the atomic PDR. Indeed, the observed evolution of the AIB emission and profiles across the Bar implies that small PAHs, aliphatic side groups, and very small carbonaceous grains undergo photodestruction in the atomic PDR (Peeters et al. 2024; Schroetter et al. 2024; Chown et al. 2024; Pasquini et al. 2024, Scheffer et al., in prep., Khan et al. in prep.).

Laboratory experiments show that the photodestruction of PAHs produces C_2H_2 (acetylene) as main carbon-bearing fragment (Jochims et al. 1994; Ekern et al. 1998; Zhen et al. 2015). Given that the photodissociation of C_2H_2 produces C_2H (see Fig. 11; Cheng et al. 2011; Heays et al. 2017), this process may explain the presence of C_2H in the atomic PDR. In addition, experiments show that photodissociation of aliphatic PAHs produce hydrocarbons such as CH_x , C_2H_x , and C_3H_x (Marciniak et al. 2021). However, the aliphatic content of the AIB carriers in the atomic PDR is small, with the ratio of carbon atoms in aliphatic units to those in aromatic rings being approximately $< 1\%$ (see next section). Finally, experiments also show that the photolysis of hydrogenated amorphous carbon (HAC) grains leads to the production of a large variety of hydrocarbon molecules, in particular methane (CH_4), and, to a lesser extent, C_2H_x and C_3H_x (e.g., Alata et al. 2014; Duley et al. 2015).

Overall, photolysis of aliphatic PAHs, small PAHs, and HAC grains may inject hydrocarbons and temporarily increase their abundance in a PDR (e.g., Awad & Viti 2022). However, in a strongly irradiated PDR, the timescale of this photoprocessing is short ($\sim 10^3$ yr; Jones et al. 2014), and the subsequent photodissociation of any daughter molecular fragments much faster. These time-scales contrast with the crossing time of $t_c \approx 3 \times 10^4$ yr for material advected from the molecular PDR to the atomic PDR, at $\sim 1 \text{ km s}^{-1}$ in the Bar (Pabst et al. 2019).

To be more quantitative, Murga et al. (2020) developed a model of the Bar simulating the photoprocessing of PAHs. In Murga's model (their Fig. A.2), enhanced C_2H_2 abundances due to the photodestruction of PAHs occur in the atomic PDR ($A_V < 1$ mag), but over short timescales ($\sim 10^4$ yr $< t_c$). However, the resulting increase in C_2H abundance is small, likely because molecular fragments quickly photodissociate and most gas-phase carbon quickly converts into C and C^+ . Murga et al. (2023) also developed a time-dependent model of HAC photodestruction (leading to CH_4 and other fragments) adapted to the strong FUV-illumination conditions of the Bar. In their model, HAC photodestruction does not dominate either, and cannot explain the observed abundances of C_2H (this work) or of other small hydrocarbons detected by Cuadrado et al. (2015). Only in the atomic PDR zone (at $A_V \approx 0.1$ mag) was this process found to produce a modest C_2H abundance ($\lesssim 10^{-10}$; Murga et al. 2023).

We conclude that photodestruction of PAHs or HAC grains may explain the transient presence of trace amounts of C_2H in the atomic PDR, assuming that PAHs and HAC grains are continually replenished (e.g., by evaporating very small grains, Pilleri et al. 2012) or quickly advected from the molecular cloud. These top-down processes may also contribute to the production of heavier hydrocarbons (with more than two C atoms) elsewhere in the PDR (e.g., Alata et al. 2015). However, our non-detection of C_2H_2 and CH_4 (the main hydrocarbon products of PAH and carbon grain photolysis) with JWST makes it difficult to predict their contribution.

6.3. Are hydrocarbon radicals and aliphatic PAHs linked?

Previous observations revealed the decrease of the 3.4/3.3 μm AIB intensity ratio with increasing FUV flux in PDRs (Geballe et al. 1989; Joblin et al. 1996; Sloan et al. 1997; Mori et al. 2014; Pilleri et al. 2015). This evolution is consistent with the photo-destruction of the more fragile bonds associated to the 3.4 μm band carriers (e.g., Marciniak et al. 2021). With JWST, we spatially resolve the evolution of the 3.4/3.3 μm AIB ratio, which shows a particularly low value in the Orion Bar (a high G_0 PDR), ranging from ~ 0.1 in DF3 to ~ 0.04 in the atomic PDR (Peeters et al. 2024; Chown et al. 2024; Pasquini et al. 2024). These values imply that the aliphatic component of the AIB carriers is small, comprising only $\sim 2\%$ (DF3) to $\sim 0.5\%$ (atomic PDR) of the carbon atoms in aliphatic groups compared to those in aromatic rings (assuming plausible band strengths for the 3.3 and 3.4 μm bands; e.g., Yang et al. 2013, 2016).

In the DFs, the spatial distribution of the C_2H emission closely resembles the observed peaks of the 3.4/3.3 μm AIB ratio (Figs. 6 and 7). This striking similarity may suggest a causal relationship between the abundance peaks of hydrocarbon radicals and an increased proportion of PAHs with aliphatic side groups responsible for the ~ 3.4 μm AIB (Duley & Williams 1981; Jourdain de Muizon et al. 1986, 1990; Joblin et al. 1996). Our PDR models show that the high abundance of C_2H (and that of CH, CH_2 , and CH_3) in the DFs can be attributed solely to gas-phase reactions initiated by C^+ and H_2^+ . In the DFs, the abundance of these simple hydrocarbons (all together) is greater than the abundance of typical PAHs containing ~ 50 C atoms (a few 10^{-7} with respect to H nuclei; e.g., Tielens 2008). Therefore, it is conceivable that highly reactive and abundant radicals react *in situ* with PAHs, leading to PAHs with a small number of aliphatic side groups (e.g., methylated PAHs; Joblin et al. 1996) and promoting the formation of additional aromatic rings (e.g., reactions with C_2H) which increases the size of the emitting PAHs. The recent detection of CN-radical derivatives of simple PAHs in TMC-1, such as naphthalene ($C_{10}H_8$; McGuire et al. 2021), acenaphthylene ($C_{12}H_8$; Cernicharo et al. 2024), and pyrene ($C_{16}H_{10}$; Wenzel et al. 2024a,b), signals the importance of bottom-up gas-phase routes (e.g., Kaiser et al. 2015; Reizer et al. 2022), as CN radicals react readily with aromatic species (e.g., Heitkämper et al. 2022; Wenzel et al. 2024b).

Chemical and laboratory experiments globally support this view (e.g., Lemmens et al. 2022) as indeed they demonstrate that PAHs react with simple hydrocarbon radicals such as CH (Soorkia et al. 2010; Goulay et al. 2006; Reilly et al. 2018; He et al. 2020), CH_2 (Kraus et al. 1993), CH_3 (Shukla et al. 2010; Zhao et al. 2019; Levey et al. 2022), and C_2H (Goulay & Leone 2006; Mebel et al. 2008). Some of these reactions may only be relevant in high-temperature chemistry (e.g., the Bar), others can exhibit a positive temperature dependence but be efficient at low temperature (e.g., Reizer et al. 2022). We conclude that *in-situ* reactions between simple but very abundant hydrocarbon radicals and PAHs may locally contribute to increase the aliphatic content of the AIB carriers in PDRs (regardless of what the initial content was). This bottom-up radical chemistry is then balanced, when PAHs are exposed to strong FUV fields, by photolysis of the aliphatic side groups, which reduces the 3.4/3.3 μm AIB ratio.

In dark clouds, most PAHs likely freeze out on grains due to their large binding energies, and thus high condensation temperatures (greater than that of water; Piacentino et al. 2024). Experiments show that photolysis of PAHs in ices containing CH_4 result in methylation of these PAHs (Bernstein et al. 2002). In the Bar, the 3.4 / 3.3 μm AIB ratio decreases again behind DF3 (Fig. 7),

but much less steeply than the C₂H emission (which reflects the sharp reduction in gas-phase hydrocarbon formation). We hypothesize that the photodesorption of methylated PAHs from ices contributes to the increasing 3.4/3.3 μm ratio in this deeper PDR zone. This may be a relevant mechanism in low-illumination PDRs due to colder grains and less efficient gas-phase hydrocarbon production compared to strongly irradiated PDRs (Fig. 12).

7. Summary and conclusions

We summarize our results as follows:

- The rim of the Bar shows a corrugated, filamentary, and turbulent structure made of small-scale dissociation fronts that are bright and remarkably similar in both IR H₂ and submm C₂H 4–3 emission. These fronts are engulfed in a PAH-emitting halo that separates the neutral, predominantly atomic edge of the PDR from the adjacent H II region. The distribution of the C¹⁸O 3–2 emission is less filamentary but more clumpy, and peaks deeper inside the molecular cloud (Sect. 3). The [C I] 609 μm emission peaks very close (≤ 0.002 pc) to the main DFs, suggesting molecular gas structures with density gradients (Sect. 3).

- The C₂H $N=4-3$ emission traces hydrocarbon radical peaks in the DFs, slightly ahead of the CO/C transition, characterized by remarkably high C₂H abundances, reaching up to several $\times 10^{-7}$ relative to H. The C₂H emission profile more closely follows the IR H₂ emission than the gas temperature profile (Sect. 4).

- The high abundance of C₂H (and related radicals CH₃, CH₂, and CH) at these peaks can be explained by simple gas-phase reactions, driven by elevated temperatures, the presence of C⁺ and C, and the enhanced reactivity of FUV-pumped H₂^{*} (Sect. 5). This FUV-driven gas-phase carbon chemistry is very efficient in dense PDR gas with $G_0 > 10^2$ (Sect. 6.1).

- At low A_V , in the atomic PDR zone (where $[H] \gg [H_2]$), the AIB emission is brightest, but aliphatic bonds and small PAHs are photo-destroyed (Peeters et al. 2024; Chown et al. 2024; Schroetter et al. 2024; Pasquini et al. 2024). Here, the production of hydrocarbon radicals from gas-phase reactions is negligible. Thus, the detection of trace, transient amounts of C₂H may result from top-down formation mechanisms, such as photoerosion of small PAHs and very small carbonaceous grains (Sect. 6.2).

- In the DFs, the C₂H emission peaks coincide with the peaks of the 3.4/3.3 μm AIB intensity ratio (Sect. 4.1), a proxy for the aliphatic-to-aromatic content of PAHs. This spatial coincidence implies that the conditions triggering the formation of simple hydrocarbons also favor the formation of PAHs with aliphatic side groups, potentially through bottom-up processes in which abundant CH_{*n*} radicals react *in situ* with PAHs, locally enhancing their aliphatic content. Reactions of PAHs with heavier radicals, such as C₂H, may also promote the formation of additional rings, thereby increasing the size of the emitting PAHs (Sect. 6.3).

While this study highlights the role of gas-phase chemistry and suggests bottom-up processes in FUV-irradiated gas, similar observations of hydrocarbons containing three or more carbon atoms are needed to constrain the limits of this chemistry. In addition, a more precise assignment of the carriers of the 3.4 μm emission sub-bands across different PDR positions is needed to determine the relative contributions of methylated PAHs and superhydrogenated PAHs. The latter may be relevant in higher-density regions and could form within water ice mantles upon UV irradiation (Bernstein et al. 1999). In general, combined observations of AIBs and C₂H (as a proxy for CH_{*n*} radicals, whose rotational lines are found at less accessible wavelengths) in other PDRs will be needed to draw more quantitative conclusions.

Interestingly, this carbon photochemistry is also relevant for planet-forming disks affected by FUV (e.g., Bosman et al. 2021; Berné et al. 2023; Goicoechea et al. 2024), which boosts the abundance of simple hydrocarbons. Our study calls for dynamical PDR models with chemical networks that gradually incorporate PAH formation, destruction, reactivity (e.g., with radicals, atoms, and H₂^{*}), and the photodesorption of frozen PAHs. Still, many reaction pathways remain uncharacterized, making much more theoretical and laboratory work necessary.

Acknowledgements. We thank our referee for a concise but constructive report. We made use of ADS/JAO.ALMA#2021.1.01369.S data. ALMA is a partnership of ESO (representing its member states), NSF (USA) and NINS (Japan), together with NRC (Canada), NSTC and ASIAA (Taiwan), and KASI (Republic of Korea), in cooperation with the Republic of Chile. The Joint ALMA Observatory is operated by ESO, AUI/NRAO and NAOJ. The JWST data were obtained from the Mikulski Archive for Space Telescopes at the Space Telescope Science Institute, which is operated by the Association of Universities for Research in Astronomy, Inc., under NASA contract NAS 5-03127. Support for program #1288 was provided by NASA through a grant from the Space Telescope Science Institute, which is operated by the Association of Universities for Research in Astronomy, Inc., under NASA contract NAS 5-03127. JRG, SC, and MGSM thank the Spanish MCINN for funding support under grant PID2023-146667NB-I00. We thank the PCMI of CNRS/INSU with INC/INP, co-funded by CEA and CNES. EP acknowledges support from the University of Western Ontario, the Institute for Earth and Space Exploration, the Canadian Space Agency (CSA, 22JWG01-16), and the Natural Sciences and Engineering Research Council of Canada. TO acknowledges the support by the Japan Society for the Promotion of Science KAKENHI Grant Number JP24K07087. This project has received funding from the European Research Council (ERC) under the European Union’s Horizon Europe research and innovation programme ERC-AdG-2022 (GA No. 101096293). MGSM acknowledges support from the NSF under grant CAREER 2142300.

References

- Agúndez, M., Goicoechea, J. R., Cernicharo, J., Faure, A., & Roueff, E. 2010, *ApJ*, 713, 662
- Alata, I., Cruz-Díaz, G. A., Muñoz Caro, G. M., & Dartois, E. 2014, *A&A*, 569, A119
- Alata, I., Jallat, A., Gavilan, L., et al. 2015, *A&A*, 584, A123
- Alexander, M. H., Dagdigan, P. J., Werner, H. J., et al. 2023, *Computer Physics Communications*, 289, 108761
- Allain, T., Leach, S., & Sedlmayr, E. 1996, *A&A*, 305, 616
- Allamandola, L. J., Tielens, A. G. G. M., & Barker, J. R. 1985, *ApJ*, 290, L25
- Allers, K. N., Jaffe, D. T., Lacy, J. H., Draine, B. T., & Richter, M. J. 2005, *ApJ*, 630, 368
- Andree-Labsch, S., Ossenkopf-Okada, V., & Röllig, M. 2017, *A&A*, 598, A2
- Andrews, H., Boersma, C., Werner, M. W., et al. 2015, *ApJ*, 807, 99
- Andrews, H., Candian, A., & Tielens, A. G. G. M. 2016, *A&A*, 595, A23
- Arab, H., Abergel, A., Habart, E., et al. 2012, *A&A*, 541, A19
- Asplund, M., Grevesse, N., Sauval, A. J., & Scott, P. 2009, *ARA&A*, 47, 481
- Asvany, O., Schlemmer, S., & Gerlich, D. 2004, *ApJ*, 617, 685
- Awad, Z., & Viti, S. 2022, *MNRAS*, 511, 3832
- Bakes, E. L. O., Tielens, A. G. G. M., & Bauschlicher, Charles W., J. 2001, *ApJ*, 556, 501
- Berné, O., Habart, E., Peeters, E., et al. 2024, *Science*, 383, 988
- Berné, O., Joblin, C., Deville, Y., et al. 2007, *A&A*, 469, 575
- Berné, O., Marcelino, N., & Cernicharo, J. 2014, *ApJ*, 795, 13
- Berné, O., Martin-Drumel, M.-A., Schroetter, I., et al. 2023, *Nature*, 621, 56
- Bernstein, M. P., Elsila, J. E., Dworkin, J. P., et al. 2002, *ApJ*, 576, 1115
- Bernstein, M. P., Sandford, S. A., & Allamandola, L. J. 1996, *ApJ*, 472, L127
- Bernstein, M. P., Sandford, S. A., Allamandola, L. J., et al. 1999, *Science*, 283, 1135
- Bierbaum, V. M., Le Page, V., & Snow, T. P. 2011, in *EAS Publications Series*, Vol. 46, *EAS Publications Series*, ed. C. Joblin & A. G. G. M. Tielens, 427–440
- Bosman, A. D., Alarcón, F., Zhang, K., & Bergin, E. A. 2021, *ApJ*, 910, 3
- Bron, E., Agúndez, M., Goicoechea, J. R., & Cernicharo, J. 2018, *ArXiv e-prints*
- Cardelli, J. A., Clayton, G. C., & Mathis, J. S. 1989, *ApJ*, 345, 245
- Cernicharo, J., Agúndez, M., Cabezas, C., et al. 2021, *A&A*, 649, L15
- Cernicharo, J., Cabezas, C., Fuentetaja, R., et al. 2024, *A&A*, 690, L13
- Cesarsky, D., Lequeux, J., Ryter, C., & Gérin, M. 2000, *A&A*, 354, L87
- Cheng, B.-M., Chen, H.-F., Lu, H.-C., et al. 2011, *ApJS*, 196, 3
- Chown, R., Okada, Y., Peeters, E., et al. 2025, *arXiv e-prints*, arXiv:2411.06061
- Chown, R., Sidhu, A., Peeters, E., et al. 2024, *A&A*, 685, A75
- Cuadrado, S., Goicoechea, J. R., Cernicharo, J., et al. 2017, *A&A*, 603, A124
- Cuadrado, S., Goicoechea, J. R., Pilleri, P., et al. 2015, *A&A*, 575, A82

- Cuadrado, S., Salas, P., Goicoechea, J. R., et al. 2019, *A&A*, 625, L3
- Dalgarno, A. & McCray, R. A. 1972, *ARA&A*, 10, 375
- de Graauw, T., Helmich, F. P., Phillips, T. G., et al. 2010, *A&A*, 518, L6
- Declair, M., Gordon, K. D., Andrews, J. E., et al. 2022, *ApJ*, 930, 15
- Duley, W. W. & Williams, D. A. 1981, *MNRAS*, 196, 269
- Duley, W. W., Zaidi, A., Wesolowski, M. J., & Kuzmin, S. 2015, *MNRAS*, 447, 1242
- Ekern, S. P., Marshall, A. G., Szczepanski, J., & Vala, M. 1998, *The Journal of Physical Chemistry A*, 102, 3498
- Elyajouri, M., Ysard, N., Abergel, A., et al. 2024, *A&A*, 685, A76
- Federrath, C. & Klessen, R. S. 2013, *ApJ*, 763, 51
- Flannery, B. P., Roberge, W., & Rybicki, G. B. 1980, *ApJ*, 236, 598
- Fossé, D., Cesarsky, D., Gerin, M., Lequeux, J., & Tiné, S. 2000, in *ESA, Vol. 456, ISO Beyond the Peaks: The 2nd ISO Workshop on Analytical Spectroscopy*, ed. A. Salama, M. F. Kessler, K. Leech, & B. Schulz, 91
- Freeman, A. & Williams, D. A. 1982, *Ap&SS*, 83, 417
- Fuente, A., Rodríguez-Franco, A., García-Burillo, S., Martín-Pintado, J., & Black, J. H. 2003, *A&A*, 406, 899
- Fuente, A., Rodríguez-Franco, A., & Martín-Pintado, J. 1996, *A&A*, 312, 599
- Fuente, A., Roueff, E., Le Petit, F., et al. 2024, *A&A*, 687, A87
- García-Burillo, S., Viti, S., Combes, F., et al. 2017, *A&A*, 608, A56
- Geballe, T. R., Tielens, A. G. G. M., Allamandola, L. J., Moorhouse, A., & Brand, P. W. J. L. 1989, *ApJ*, 341, 278
- Gerin, M., Neufeld, D. A., & Goicoechea, J. R. 2016, *ARA&A*, 54, 181
- Glover, S. C. O. & Mac Low, M. M. 2011, *MNRAS*, 412, 337
- Goicoechea, J. R. & Cuadrado, S. 2021, *A&A*, 647, L7
- Goicoechea, J. R. & Le Bourlot, J. 2007, *A&A*, 467, 1
- Goicoechea, J. R., Le Bourlot, J., Black, J. H., et al. 2024, *A&A*, 689, L4
- Goicoechea, J. R., Lique, F., & Santa-Maria, M. G. 2022, *A&A*, 658, A28
- Goicoechea, J. R., Pabst, C. H. M., Kabanovic, S., et al. 2020, *A&A*, 639, A1
- Goicoechea, J. R., Pety, J., Cuadrado, S., et al. 2016, *Nature*, 537, 207
- Goicoechea, J. R. & Roncero, O. 2022, *A&A*, 664, A190
- Goicoechea, J. R., Santa-Maria, M. G., Bron, E., et al. 2019, *A&A*, 622, A91
- Goicoechea, J. R., Teyssier, D., Etaluzze, M., et al. 2015, *ApJ*, 812, 75
- Gordon, K. D., Clayton, G. C., Declair, M., et al. 2023, *ApJ*, 950, 86
- Gorti, U. & Hollenbach, D. 2002, *ApJ*, 573, 215
- Goulay, F. & Leone, S. R. 2006, *The Journal of Physical Chemistry A*, 110, 1875, pMID: 16451020
- Goulay, F., Rebrion-Rowe, C., Biennier, L., et al. 2006, *The Journal of Physical Chemistry A*, 110, 3132, pMID: 16509636
- Guzmán, V. V., Pety, J., Goicoechea, J. R., et al. 2015, *ApJ*, 800, L33
- Habart, E., Le Gal, R., Alvarez, C., et al. 2023, *A&A*, 673, A149
- Habart, E., Peeters, E., Berné, O., et al. 2024, *A&A*, 685, A73
- Hartmann, L. & Burkert, A. 2007, *ApJ*, 654, 988
- He, C., Thomas, A. M., Galimova, G. R., et al. 2020, *Journal of the American Chemical Society*, 142, 3205, pMID: 31961149
- Heays, A. N., Bosman, A. D., & van Dishoeck, E. F. 2017, *A&A*, 602, A105
- Heitkampfer, J., Suchanek, S., García de la Concepción, J., Kästner, J., & Molpeceres, G. 2022, *Frontiers in Astronomy and Space Sciences*, 9, 347
- Hernández, M. I., Tejada, G., Fernández, J. M., & Montero, S. 2021, *A&A*, 647, A155
- Hierl, P. M., Morris, R. A., & Viggiano, A. A. 1997, *J. Chem. Phys.*, 106, 10145
- Hill, J. K. & Hollenbach, D. J. 1978, *ApJ*, 225, 390
- Hollenbach, D., Kaufman, M. J., Bergin, E. A., & Melnick, G. J. 2009, *ApJ*, 690, 1497
- Joblin, C. 2003, in *SF2A-2003: Semaine de l'Astrophysique Française*, ed. F. Combes, D. Barret, T. Contini, & L. Pagani, 175
- Joblin, C., Bron, E., Pinto, C., et al. 2018, *A&A*, 615, A129
- Joblin, C., Tielens, A. G. G. M., Allamandola, L. J., & Geballe, T. R. 1996, *ApJ*, 458, 610
- Jochims, H. W., Ruhl, E., Baumgartel, H., Tobita, S., & Leach, S. 1994, *ApJ*, 420, 307
- Jones, A. P. 2012, *A&A*, 540, A1
- Jones, A. P., Ysard, N., Köhler, M., et al. 2014, *Faraday Discussions*, 168, 313
- Jourdain de Muizon, M., D'Hendecourt, L. B., & Geballe, T. R. 1990, *A&A*, 235, 367
- Jourdain de Muizon, M., Geballe, T. R., D'Hendecourt, L. B., & Baas, F. 1986, *ApJ*, 306, L105
- Kaiser, R. I., Parker, D. S., & Mebel, A. M. 2015, *Annual Review of Physical Chemistry*, 66, 43
- Kaplan, K. F., Dinerstein, H. L., Kim, H., & Jaffe, D. T. 2021, *ApJ*, 919, 27
- Klos, J., Bergeat, A., Vanuzzo, G., et al. 2018, *The Journal of Physical Chemistry Letters*, 9, 6496
- Klos, J., Bergeat, A., Vanuzzo, G., et al. 2019, *The Journal of Physical Chemistry Letters*, 10, 3408, pMID: 31181935
- Kraus, H., Oehlers, C., Temps, F., & Wagner, H. G. 1993, *The Journal of Physical Chemistry*, 97, 10989
- Le Page, V., Snow, T. P., & Bierbaum, V. M. 2003, *ApJ*, 584, 316
- Le Petit, F., Nehmé, C., Le Bourlot, J., & Roueff, E. 2006, *ApJS*, 164, 506
- Leger, A. & Puget, J. L. 1984, *A&A*, 137, L5
- Lemmens, A. K., Rap, D. B., Brünken, S., Buma, W. J., & Rijs, A. M. 2022, *Physical Chemistry Chemical Physics*, 24, 14816
- Levey, Z. D., Laws, B. A., Sundar, S. P., et al. 2022, *The Journal of Physical Chemistry A*, 126, 101, pMID: 34936357
- Li, A. & Draine, B. T. 2012, *ApJ*, 760, L35
- Lis, D. C. & Schilke, P. 2003, *ApJ*, 597, L145
- Luhman, M. L., Jaffe, D. T., Keller, L. D., & Pak, S. 1994, *ApJ*, 436, L185
- Maillard, V., Bron, E., & Le Petit, F. 2021, *A&A*, 656, A65
- Marciniak, A., Joblin, C., Mulas, G., Mundlapati, V. R., & Bonnamy, A. 2021, *A&A*, 652, A42
- Marconi, A., Testi, L., Natta, A., & Walmsley, C. M. 1998, *A&A*, 330, 696
- Mazo-Sevillano, P. d., Aguado, A., Goicoechea, J. R., & Roncero, O. 2024, *The Journal of Chemical Physics*, 160, 184307
- McGuire, B. A., Burkhardt, A. M., Kalenskii, S., et al. 2018, *Science*, 359, 202
- McGuire, B. A., Loomis, R. A., Burkhardt, A. M., et al. 2021, *Science*, 371, 1265
- Mebel, A. M., Kislov, V. V., & Kaiser, R. I. 2008, *Journal of the American Chemical Society*, 130, 13618, pMID: 18795780
- Meier, D. S., Walter, F., Bolatto, A. D., et al. 2015, *ApJ*, 801, 63
- Montillaud, J., Joblin, C., & Toubanc, D. 2013, *A&A*, 552, A15
- Mori, T. I., Onaka, T., Sakon, I., et al. 2014, *ApJ*, 784, 53
- Murga, M. S., Kirsanova, M. S., Vasyunin, A. I., & Pavlyuchenkov, Y. N. 2020, *MNRAS*, 497, 2327
- Murga, M. S., Vasyunin, A. I., & Kirsanova, M. S. 2023, *MNRAS*, 519, 2466
- Nagy, Z., Choi, Y., Ossenkopf-Okada, V., et al. 2017, *A&A*, 599, A22
- Nagy, Z., Ossenkopf, V., Van der Tak, F. F. S., et al. 2015, *A&A*, 578, A124
- Nagy, Z., Van der Tak, F. F. S., Ossenkopf, V., et al. 2013, *A&A*, 550, A96
- Naylor, D. A., Dartois, E., Habart, E., et al. 2010, *A&A*, 518, L117
- Neufeld, D. A. 2012, *ApJ*, 749, 125
- O'Dell, C. R. 2001, *ARA&A*, 39, 99
- Ossenkopf, V., Röllig, M., Neufeld, D. A., et al. 2013, *A&A*, 550, A57
- Pabst, C., Higgins, R., Goicoechea, J. R., et al. 2019, *Nature*, 565, 618
- Pabst, C. H. M., Goicoechea, J. R., Cuadrado, S., et al. 2024, *A&A*, 688, A7
- Pabst, C. H. M., Goicoechea, J. R., Teyssier, D., et al. 2020, *A&A*, 639, A2
- Parikka, A., Habart, E., Bernard-Salas, J., et al. 2017, *A&A*, 599, A20
- Parmar, P. S., Lacy, J. H., & Achtermann, J. M. 1991, *ApJ*, 372, L25
- Pasquini, S., Peeters, E., Scheffter, B., et al. 2024, *A&A*, 685, A77
- PDRs4All-Team, Berné, O., Émilie Habart, et al. 2022, *Publications of the Astronomical Society of the Pacific*, 134, 054301
- Peeters, E., Habart, E., Berné, O., et al. 2024, *A&A*, 685, A74
- Peeters, E., Hony, S., Van Kerckhoven, C., et al. 2002, *A&A*, 390, 1089
- Pellegrini, E. W., Baldwin, J. A., Ferland, G. J., Shaw, G., & Heathcote, S. 2009, *ApJ*, 693, 285
- Pety, J., Gratier, P., Guzmán, V., et al. 2012, *A&A*, 548, A68
- Pety, J. & Rodríguez-Fernández, N. 2010, *A&A*, 517, A12+
- Pety, J., Teyssier, D., Fossé, D., et al. 2005, *A&A*, 435, 885
- Piacentino, E. L., Balkanski, A., Rajappan, M., & Oberg, K. I. 2024
- Pillari, P., Joblin, C., Boulanger, F., & Onaka, T. 2015, *A&A*, 577, A16
- Pillari, P., Montillaud, J., Berné, O., & Joblin, C. 2012, *A&A*, 542, A69
- Pillari, P., Treviño-Morales, S., Fuente, A., et al. 2013, *A&A*, 554, A87
- Piriot Jankowiak, P., Lique, F., & Dagdigan, P. J. 2023, *MNRAS*, 526, 885
- Pitts, W. M., Pasternack, L., & McDonald, J. R. 1982, *Chemical Physics*, 68, 417
- Plomp, V., Wang, X.-D., Klos, J., et al. 2024, *The Journal of Physical Chemistry Letters*, 15, 4602
- Polehampton, E. T., Menten, K. M., Brünken, S., Winnewisser, G., & Baluteau, J. P. 2005, *A&A*, 431, 203
- Putaud, T., Michaut, X., Le Petit, F., Roueff, E., & Lis, D. C. 2019, *A&A*, 632, A8
- Reilly, N. J., da Silva, G., Wilcox, C. M., et al. 2018, *The Journal of Physical Chemistry A*, 122, 1261, pMID: 29332391
- Reizer, E., Viskolcz, B., & Fiser, B. 2022, *Chemosphere*, 291, 132793
- Rodríguez-Fernández, N., Pety, J., & Gueth, F. 2008, Single-dish observation and processing to produce the short-spacing information for a millimeter interferometer, Tech. rep., IRAM Memo 2008-2
- Roelfsema, P. R., Helmich, F. P., Teyssier, D., et al. 2012, *A&A*, 537, A17
- Salgado, F., Berné, O., Adams, J. D., et al. 2016, *ApJ*, 830, 118
- Santa-Maria, M. G., Goicoechea, J. R., Pety, J., et al. 2023, *A&A*, 679, A4
- Schroder, K., Staemmler, V., Smith, M. D., Flower, D. R., & Jaquet, R. 1991, *Journal of Physics B Atomic Molecular Physics*, 24, 2487
- Schroetter, I., Berné, O., Joblin, C., et al. 2024, *A&A*, 685, A78
- Schutte, W. A., Tielens, A. G. G. M., & Allamandola, L. J. 1993, *ApJ*, 415, 397
- Shaw, G., Ferland, G. J., Henney, W. J., et al. 2009, *ApJ*, 701, 677
- Shiozaki, T., Knizia, G., & Werner, H.-J. 2011, *J. Chem. Phys.*, 134, 034113
- Shukla, B., Miyoshi, A., & Koshi, M. 2010, *Journal of the American Society for Mass Spectrometry*, 21, 534
- Sloan, G. C., Bregman, J. D., Geballe, T. R., Allamandola, L. J., & Woodward, E. 1997, *ApJ*, 474, 735
- Smith, D., Adams, N. G., & Alge, E. 1982, *The Journal of Chemical Physics*, 77, 1261
- Sofia, U. J., Lauroesch, J. T., Meyer, D. M., & Cartledge, S. I. B. 2004, *ApJ*, 605, 272

- Soorkia, S., Taatjes, C. A., Osborn, D. L., et al. 2010, *Physical Chemistry Chemical Physics (Incorporating Faraday Transactions)*, 12, 8750
- Stecher, T. P. & Williams, D. A. 1972, *ApJ*, 177, L141
- Sternberg, A. & Dalgarno, A. 1995, *ApJS*, 99, 565
- Stoerzer, H., Stutzki, J., & Sternberg, A. 1995, *A&A*, 296, L9
- Tajuelo-Castilla, G., Mendieta-Moreno, J. I., Accolla, M., et al. 2024, *ApJ*, 965, 184
- Tauber, J. A., Lis, D. C., Keene, J., Schilke, P., & Buettgenbach, T. H. 1995, *A&A*, 297, 567
- Teyssier, D., Fossé, D., Gerin, M., et al. 2004, *A&A*, 417, 135
- Tielens, A. G. G. M. 2008, *ARA&A*, 46, 289
- Tielens, A. G. G. M. & Hollenbach, D. 1985, *ApJ*, 291, 722
- Tielens, A. G. G. M., Meixner, M. M., van der Werf, P. P., et al. 1993, *Science*, 262, 86
- Tiwari, M., Menten, K. M., Wyrowski, F., et al. 2019, *A&A*, 626, A28
- Van De Putte, D., Meshaka, R., Trahin, B., et al. 2024, *A&A*, 687, A86
- van der Werf, P. P., Goss, W. M., & O'Dell, C. R. 2013, *ApJ*, 762, 101
- van der Wiel, M. H. D., van der Tak, F. F. S., Ossenkopf, V., et al. 2009, *A&A*, 498, 161
- Veselinova, A., Agúndez, M., Goicoechea, J. R., et al. 2021, *A & A*, 648, A76
- Wan, Y., Yang, B. H., Stancil, P. C., et al. 2018, *ApJ*, 862, 132
- Wenzel, G., Cooke, I. R., Changala, P. B., et al. 2024a
- Wenzel, G., Speak, T. H., Changala, P. B., et al. 2024b
- Wolfire, M. G., Vallini, L., & Chevance, M. 2022, *ARA&A*, 60, 247
- Wyrowski, F., Schilke, P., Hofner, P., & Walmsley, C. M. 1997, *ApJ*, 487, L171
- Yang, X. J., Glaser, R., Li, A., & Zhong, J. X. 2013, *ApJ*, 776, 110
- Yang, X. J., Li, A., Glaser, R., & Zhong, J. X. 2016, *ApJ*, 825, 22
- Zanchet, A., Godard, B., Bulut, N., et al. 2013, *ApJ*, 766, 80
- Zanchet, A., Lique, F., Roncero, O., Goicoechea, J. R., & Bulut, N. 2019, *A&A*, 626, A103
- Zannese, M., Tabone, B., Habart, E., et al. 2025, arXiv e-prints, arXiv:2502.08354
- Zhao, L., Kaiser, R. I., Lu, W., et al. 2019, *Nature Communications*, 10, 3689
- Zhen, J., Castellanos, P., Paardekooper, D. M., et al. 2015, *ApJ*, 804, L7

¹ Instituto de Física Fundamental (CSIC). Calle Serrano 121-123, 28006, Madrid, Spain. e-mail: javier.r.goicoechea@csic.es

² Institut de Radioastronomie Millimétrique, 38406, Saint Martin d'Hères, France.

³ LUX, Observatoire de Paris, Université PSL, Sorbonne Université, CNRS, 75014, Paris, France.

⁴ Institut de Recherche en Astrophysique et Planétologie, Université de Toulouse, CNRS, CNES, Toulouse, France.

⁵ Institut des Sciences Moléculaires d'Orsay, CNRS, Université Paris-Saclay, Orsay, France.

⁶ Joint Quantum Institute, Department of Physics, University of Maryland, College Park, MD 20742, USA.

⁷ Dept. of Physics, Temple University, Philadelphia, PA 19122, USA.

⁸ Univ. Rennes, CNRS, IPR (Institut de Physique de Rennes), UMR6251, 35000, Rennes, France.

⁹ Department of Astronomy, Graduate School of Science, The University of Tokyo, 7-3-1 Bunkyo-ku, Tokyo 113-0033, Japan.

¹⁰ Department of Physics and Astronomy, University of Western Ontario, London, Ontario, Canada.

¹¹ Institute for Earth and Space Exploration, University of Western Ontario, London, Ontario, Canada.

¹² Carl Sagan Center, SETI Institute, Mountain View, CA, USA.

¹³ Leiden Observatory, Leiden University, Leiden, The Netherlands.

¹⁴ Astronomy Dept., University of Maryland, College Park, MD, USA.

¹⁵ Dipartimento di Fisica, Università degli Studi di Milano, Via Celoria 16, 20133 Milano, Italy.

¹⁶ LUX, Observatoire de Paris, Université PSL, Sorbonne Université, CNRS, 92190, Meudon, France.

¹⁷ Laboratoire d'Astrophysique de Bordeaux, Université de Bordeaux, CNRS, F-33615 Pessac, France.

¹⁸ Department of Astronomy, The Ohio State University, 140 West 18th Avenue, Columbus, OH 43210, USA.

¹⁹ Centro de Astrobiología (CAB), CSIC-INTA, Ctra. de Torrejón a Ajalvir, km 4, 28850 Torrejón de Ardoz, Spain.

²⁰ Université Paris-Saclay, CNRS, Institut d'Astrophysique Spatiale, Orsay, France.

²¹ Department of Astronomy, University of Florida, P.O. Box 112055, Gainesville, FL 32611, USA.

Appendix A: Source coordinates

Table A.1. Coordinates of main sources in the Bar.

Source	$\alpha(2000)$	$\delta(2000)$	Comment
DF1	5:35:20.51	-5:25:11.95	Dissociation front
DF2	5:35:20.62	-5:25:14.71	Dissociation front
DF3	5:35:20.75	-5:25:20.56	Dissociation front
DF4	5:35:19.35	-5:25:28.20	Dissociation front
d203-506	5:35:20.32	-5:25:05.55	Irradiated disk

Appendix B: Beam dilution in single-dish observations: beam coupling factors

To approximately correct for single-dish beam-size differences, we estimated a frequency-dependent beam coupling factor (f_b) using the spatial information provided by the high-angular resolution C_2H $N=4-3$ map taken with ALMA. In doing this, we assume that the emission from all C_2H rotational lines have the same spatial distribution. We correct the observed integrated line intensities, I_{obs} , measured by the IRAM 30 m and Herschel telescopes as: $I_{corr} = I_{obs}/f_b$. We do this in a two step procedure. We first spatially smoothed the large C_2H $N=4-3$ map obtained with the IRAM 30 m telescope to the different full width at half maximum (FWHM) beam at the frequency of each C_2H rotational line observed in the IRAM 30 m and Herschel/HIFI line surveys toward the SDLS position. We then compute $f_b(\text{single-dish}) = I_{smooth}(\text{HPBW})/I_{obs}(8'')$, where $I_{smooth}(\text{HPBW})$ is the intensity (in $K \text{ km s}^{-1}$) of the C_2H $N=4-3$ line extracted from the spatially smoothed maps toward the SDLS position. In a second step, we smoothed the high angular resolution ALMA C_2H $N=4-3$ map to a $8''$ angular resolution and compute $f_b(\text{ALMA}) = I_{smooth}(8'')/I_{obs}(\text{ALMA})$, where $I_{smooth}(8'')$ is the intensity of the C_2H $N=4-3$ line extracted from the smoothed ALMA maps toward the SDLS position. The final beam coupling correction factor is $f_b = f_b(\text{single-dish}) \cdot f_b(\text{ALMA})$. The resulting correction factors are listed in Table B.1.

Table B.1. Beam coupling corrections and C₂H line intensities toward the SDLS position (Fig. 1 left).

Species	Frequency [GHz]	Telescope / Receiver	HPBW [arcsec]				I_{corr}^a [K km s ⁻¹]
				$f_b(\text{single-dish})$	$f_b(\text{ALMA})$	$f_b(\text{total})$	
C ₂ H $N = 1 - 0$	87.3	IRAM 30m/E0	28.2	0.76	0.89	0.67	13.5
C ₂ H $N = 2 - 1$	174.7	IRAM 30m/E1	14.1	0.93	0.89	0.83	28.4
C ₂ H $N = 3 - 2$	262.0	IRAM 30m/E2	9.4	0.99	0.89	0.88	38.7
C ₂ H $N = 4 - 3$	349.3	IRAM 30m/E3	8.0	1.00	0.89	0.89	37.0
C ₂ H $N = 6 - 5$	524.0	Herschel/HIFI	40.5	0.66	0.89	0.59	13.7
C ₂ H $N = 7 - 6$	611.3	Herschel/HIFI	34.7	0.70	0.89	0.62	8.7
C ₂ H $N = 8 - 7$	698.5	Herschel/HIFI	30.4	0.74	0.89	0.66	4.7
C ₂ H $N = 9 - 8$	785.8	Herschel/HIFI	27.0	0.77	0.89	0.68	3.6
C ₂ H $N = 10 - 9$	873.1	Herschel/HIFI	24.3	0.80	0.89	0.71	3.6

Notes. In this work we correct the observed C₂H line intensities obtained with the IRAM 30 m and Herschel telescopes toward the SDLS position as $I_{\text{corr}} = I_{\text{obs}} / f_b(\text{total})$, with $f_b(\text{total}) = f_b(\text{single-dish}) \cdot f_b(\text{ALMA})$. $I_{\text{obs}}(\text{IRAM})$ are taken from Cuadrado et al. (2015). $I_{\text{obs}}(\text{HIFI})$ are taken from Table A.1 of Nagy et al. (2017). ^aAdding the intensities of all individual fine-structure and hyperfine-structure C₂H lines.

Appendix C: Complementary observational figures

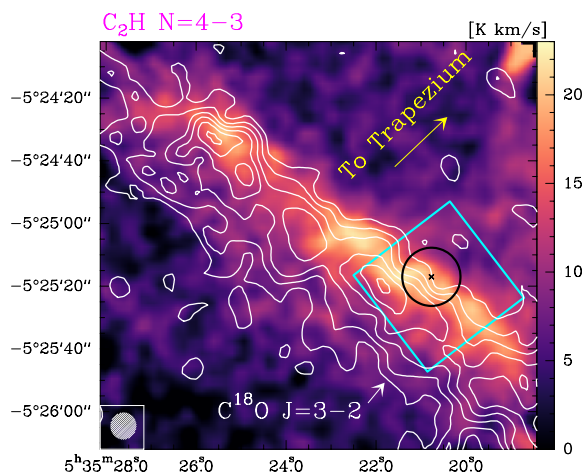


Fig. C.1. IRAM 30m map of the entire Orion Bar in the C_2H 4–3 integrated line emission at $\sim 8''$ resolution (in R.A. and DEC. coordinates). White contours show the $C^{18}O$ 3–2 emission from 10 to 35 $K km s^{-1}$ in steps of 5 $K km s^{-1}$. The cyan square shows the FoV observed with ALMA. The black circle shows the single-dish line survey position (SDLS, Cuadrado et al. 2015) including the FoV observed with JWST.

In this Appendix we present additional images that help to better understand the relationships between the emission from different species across the Bar. Figure C.1 shows a large view of the entire Bar as seen in the C_2H $N = 4-3$ emission mapped with the IRAM 30m telescope. This emission traces an extended ridge of multiple DFs along the Bar. White contours show the $C^{18}O$ 3–2 emission tracing the more FUV-shielded molecular cloud and dense clumps.

Figure C.2 [C I] 609 μm emission velocity-centroids obtained from a two-Gaussian fit across cut A (ALMA observations).

Figure C.3 shows images of the edge of the Bar combining ALMA and JWST observations. These images reveal the small-scale structure and chemical stratification of the PDR.

Figure C.4 shows intensity-weighted mean LSR velocity maps (moment 1 maps) of the C_2H $N = 4-3$, [C I] 609 μm , and $C^{18}O$ $J = 3-2$ lines observed with ALMA. The color code is such that the greenish areas are consistent with the main emission velocities arising from the Bar PDR, reddish areas reveal slightly redshifted emission (linked to the specific gas kinematics of the PDR), whereas bluish regions mostly represent molecular gas in the background OMC-1 cloud. Toward the atomic PDR zone (to the right of the dashed vertical white line) the greenish areas may also represent gas at deeper layers of OMC-1 illuminated from a slanted angle.

Figure C.5 shows cross cut C from observations with ALMA, MIRI-MRS, and NIRSspec spectrometers. This cut crosses DF1, DF2, and DF3 (similar to Fig. 7). The dashed magenta curve shows the rotational temperature T_{64} obtained from H_2 $v = 0-0$ $S(4)$ and $S(2)$ line intensities observed with MIRI-MRS. Because of the relatively high gas densities at the DFs, $T_{64} \approx T_k$.

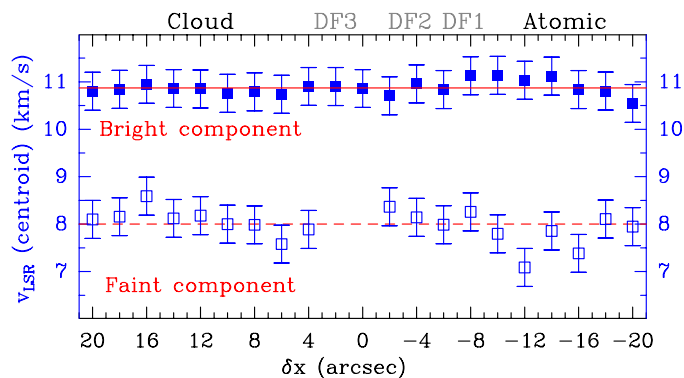


Fig. C.2. [C I] 609 μm line emission velocity-centroids obtained from a two-Gaussian fit across cut A (ALMA spectra shown in Fig. 5).

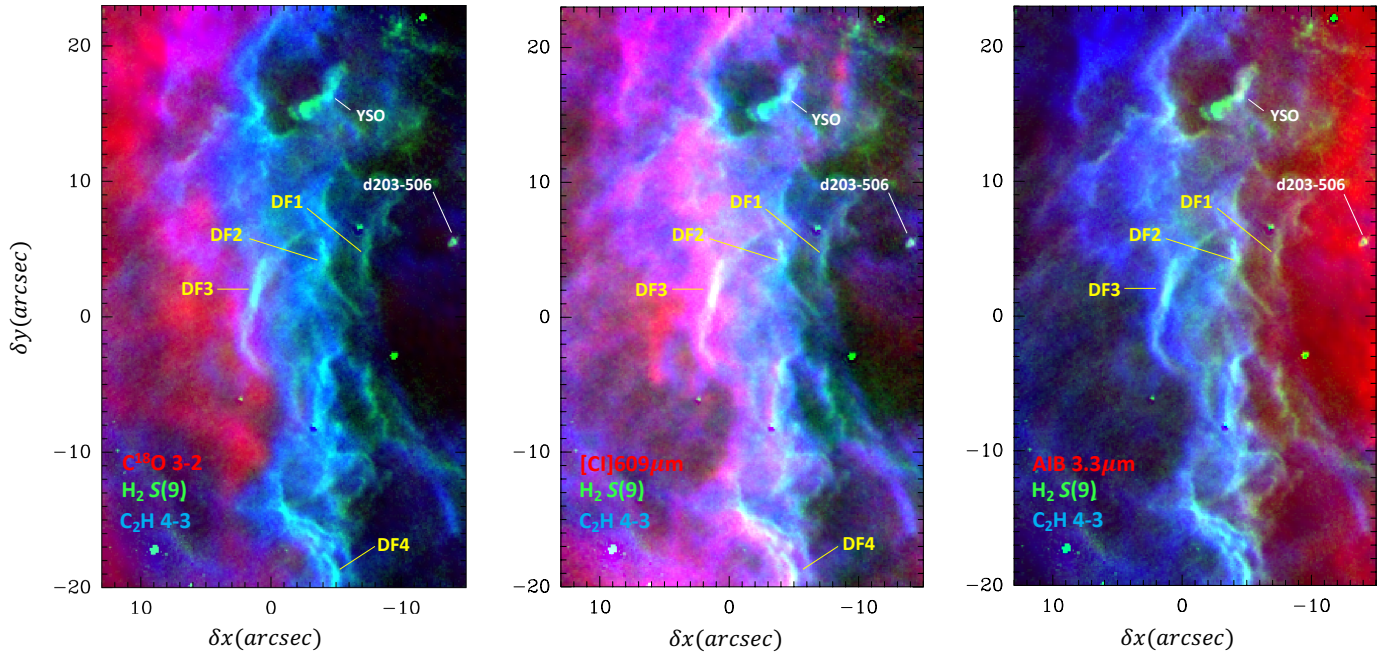


Fig. C.3. Subarcsecond resolution RGB images of the Bar. Green represents the NIRCcam F470M–F480M image (a proxy of the $\text{H}_2 v=0-0 S(9)$ emission) and blue represents the $\text{C}_2\text{H } N=4-3, F=5-4$ and $F=4-3$ emission observed with ALMA. From left to right, red represents $\text{C}^{18}\text{O } J=3-2$ observed with ALMA, $[\text{C I}] 609 \mu\text{m}$ observed with ALMA, and JWST/NIRCcam F335M–F330M image (PAH emission), respectively. We rotated the original images by 37.5° clockwise to bring the FUV illumination from the Trapezium in the horizontal direction (from the right).

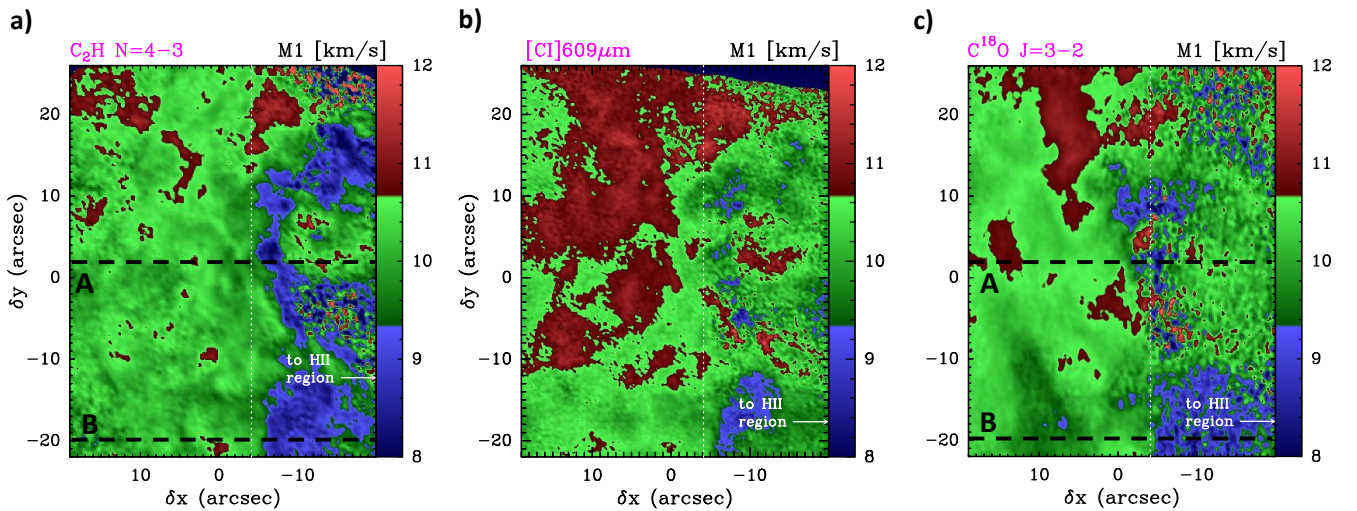


Fig. C.4. Intensity-weighted mean LSR velocity maps (moment 1): (a) $\text{C}_2\text{H } N=4-3$, (b) $[\text{C I}] 609 \mu\text{m}$, and (c) $\text{C}^{18}\text{O } J=3-2$. The green shaded areas show LSR velocities consistent with emission from the Bar. The blueish points (blue-shifted with respect to the Bar) show emission with more relevant contribution from OMC-1 in the background (e.g., DF1). The reddish points show red-shifted emission from the main velocities of the Bar PDR. We rotated the original images by 37.5° clockwise to bring the FUV illumination in the horizontal direction (from the right).

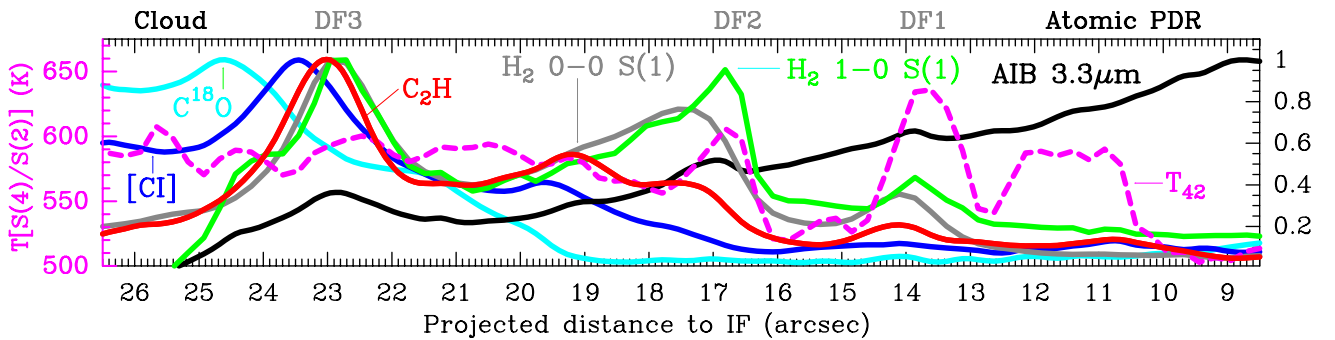


Fig. C.5. Crosscut C: vertically-averaged intensity ratio with $\Delta(\delta y) = 2''$ crossing the green cross in Fig 6. The magenta dashed line shows the rotational temperature T_{64} (scale on the left y-axis) derived from the $p\text{-H}_2 v=0-0 S(4)/S(2)$ line intensity ratio observed with MIRI-MRS (see text).

Appendix D: Line intensity correlations

To support our discussion and PDR modeling results (namely, that C_2H formation in the DFs is dominated by gas-phase chemistry initiated by reactions of C^+ with H_2^*), we constructed line-intensity correlation plots from the larger NIRCcam and Keck filter images shown in Fig. 2 (using their common $30'' \times 30''$ FoV, $\delta x = [+15'', -15'']$ and $\delta y = [-16'', +14'']$). We first spatially smoothed the images to a common angular resolution of $0.8''$. Figure D.1 shows the resulting correlation plots¹¹ after clipping intensities below a 3σ detection threshold. Blueish points show the measured line intensities in the molecular PDR, at $\delta x > -5''$ (i.e., in the DFs and deeper into the molecular cloud). The reddish points refer to the atomic PDR zone (i.e., at $\delta x < -5''$).

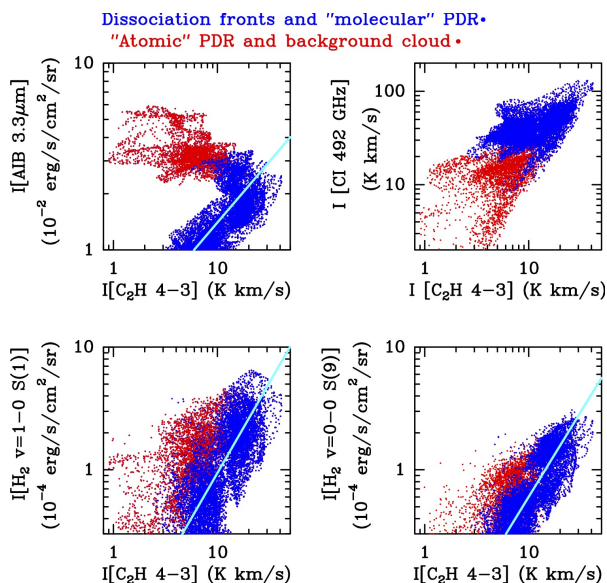


Fig. D.1. C_2H $N=4-3$ intensity correlation plots. Blueish pixels correspond to emission at $\delta x > -5''$ (main DFs and molecular PDR) whereas reddish pixels correspond to emission at $\delta x < -5''$ (atomic PDR and background OMC-1 cloud). The straight cyan lines are regression curves, with parameters of Table D.1, obtained by fitting the bluish areas only.

Table D.1 summarizes power-law fits for each correlation plot toward the molecular PDR (only taking the data in blue). To first order, the H_2 , AIB $3.3 \mu m$, and $[C\ I] 609 \mu m$ intensities monotonically follow that of C_2H $N=4-3$ (as measured by the Spearman's rank coefficient). The $I(C_2H\ 4-3)-I(H_2^*)$ intensities are the more linearly correlated ones (where the $H_2\ v=1-0\ S(1)$ and $v=0-0\ S(9)$ excited lines mostly trace FUV-pumped H_2^*).

The $I(C_2H\ 4-3)-I(C\ I\ 609 \mu m)$ plot shows that these emissions are also related, with a correlation trend that approximately extends into the atomic PDR lines-of-sight (reddish areas). That is, wherever these line intensities come from (atomic PDR or background OMC-1), they are related. Finally, the $I(C_2H\ 4-3)-I(AIB\ 3.3 \mu m)$ plot shows a different behavior, with two correlation trends: moderately correlated toward the molecular PDR (where the AIB emission is fainter), and anti-correlated toward the atomic PDR zone (where the AIB $3.3 \mu m$ band emission reaches maximum intensity values).

¹¹ The infrared images used in this correlation analysis are continuum-subtracted NIRCcam and Keck filter images (Habart et al. 2023, 2024). They represent the intensity of the AIB $3.3 \mu m$, $H_2\ v=1-0\ S(1)$, and $H_2\ v=0-0\ S(9)$ emission with an accuracy of $\lesssim 20\%$, depending on the position and environment (Chown et al. 2025). This uncertainty contributes to the scatter seen in the correlation plots (Fig. D.1).

Table D.1. Summary of the line intensity correlation plots in Fig. D.1.

x	y	a	b	ρ_P	ρ_S
$I_{C_2H\ 4-3}$	$10^2 \cdot I_{AIB\ 3.3\ \mu m}$	0.65	-0.51	0.62	0.65
$I_{C_2H\ 4-3}$	$I_{[C\ I]\ 609\ \mu m}$	0.67	0.92	0.54	0.54
$I_{C_2H\ 4-3}$	$10^4 \cdot I_{H_2\ 0-0\ S(9)}$	1.39	-1.61	0.76	0.79
$I_{C_2H\ 4-3}$	$10^4 \cdot I_{H_2\ 1-0\ S(1)}$	1.47	-1.50	0.71	0.71

Notes. Regressions fitted to the molecular PDR data (bluish areas in Fig. D.1) in a weighted least-square fit, $\log_{10} y = a \log_{10} x + b$. Coefficient ρ_P is the Pearson coefficient that measures the linearity of the log-log correlation. ρ_S is the Spearman coefficient that measures the monotonic relationship. The typical error in the fits for a and b is 0.01.

Figure D.2 shows the normalized $3.4/3.3 \mu m$ AIB ratio versus normalized $C_2H\ 4-3$ line intensity ratio extracted from the small FoV shown in Fig. 6 (the JWST spectroscopy FoV). This plot is a proxy for the increasing aliphatic content of the AIB carriers relative to the increasing column density of simple hydrocarbon radicals. The red line shows a 1:1 linear correlation.

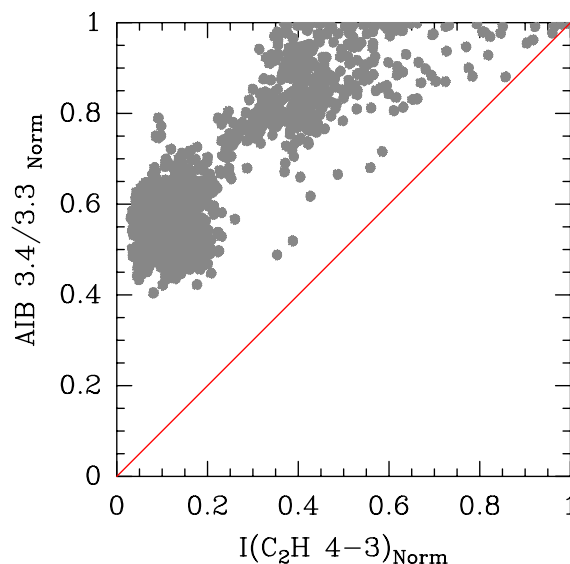


Fig. D.2. Normalized $3.4/3.3 \mu m$ AIB ratio versus normalized $C_2H\ 4-3$ line intensity ratio extracted from the small FoV in Fig. 6.

Appendix E: Nonlocal and non-LTE collisional and radiative excitation of C₂H rotational lines

In our nonlocal and non-LTE excitation and radiative transfer models (Goicoechea et al. 2022), we adopted the fine-structure resolved C₂H–H₂ rate¹² coefficients, γ_{H_2} , recently computed by Pirlot Jankowiak et al. (2023) up to C₂H rotational level $N = 20$ ($E_{up}/k = 879$ K). Hyperfine-resolved C₂H–e⁻ (Nagy et al. 2015) and C₂H–H₂ collisional rate coefficients also exist (but the latter only up to 100 K; Pirlot Jankowiak et al. 2023). We checked that for $T_k \leq 100$ K, both data sets (fine-structure versus hyperfine-structure) produce similar results. In addition, since $\gamma_{H_2} \cdot n(H_2) \gg \gamma_e \cdot n_e$, electron excitation plays negligible role for C₂H even for the highest possible e⁻ abundances near the DFs, $n_e \approx n(C^+) \approx 10^{-4} n_H$ (Cuadrado et al. 2019; Pabst et al. 2024).

In our excitation models, we include radiative excitation by absorption of dust continuum photons. We approximate this far-IR and submm continuum with a modified blackbody, with a color temperature of 50 K and a wavelength-dependent (in μm) dust continuum opacity that varies as $0.03(160/\lambda)^{1.6}$. Figure E.1 shows the synthetic continuum emission (dust and cosmic microwave background) used in our radiative transfer model. This is the continuum (external radiation and internally generated field) felt by the molecular gas in the Bar. The red dots show Herschel’s continuum measurements (Arab et al. 2012). The blue stars show the wavelength position of C₂H rotational lines.

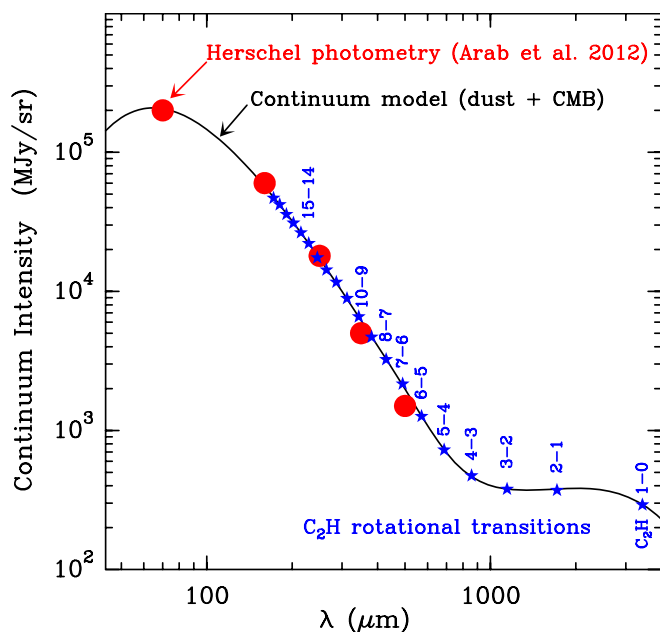


Fig. E.1. Continuum emission model (a modified black body with $T_d = 50$ K and the cosmic millimeter background) used in our C₂H excitation and radiative transfer calculations. Red circles show Herschel’s photometric measurements in the Bar (Arab et al. 2012). Blue stars show the wavelength position of the C₂H rotational transitions.

Our best models of the C₂H emission in the DFs, predict a rotational excitation temperature of $T_{rot}(C_2H\ 4-3) = 20-24$ K (subthermal excitation), in agreement with the rotational temperature inferred from a population diagram (Fig. F.1).

¹² These close-coupling quantum scattering calculations provide C₂H–o/p-H₂ inelastic rate coefficients (γ_{H_2} in $\text{cm}^3 \text{s}^{-1}$) up to $T_k = 500$ K. For higher gas temperatures, we simply extrapolate these rates as $\sqrt{T_k}$. We assume that the H₂ OTPR is thermalized to T_k , e.g., ~ 1.6 at 100 K and ~ 2.9 at 200 K.

Appendix F: C₂H rotational temperatures and $N(C_2H)$ toward the SDLS position

To understand the excitation conditions that lead to the observed (sub)mm C₂H rotational emission, we re-analyzed the C₂H $N = 1-0$ to $4-3$ (IRAM 30 m telescope, Cuadrado et al. 2015) and $N = 6-5$ to $10-9$ (Herschel/HIFI, Nagy et al. 2015, 2017) lines detected toward the single-dish line-survey (SDLS) position (see Fig. 1 left). The angular resolution of these single-dish observations varies with frequency, $\sim 8''$ to $42''$, which is not sufficient to spatially resolve the emission from the main small-scale dissociation fronts (a region of $\Delta(\delta x) \approx 10''$ width). We corrected the observed (single-dish) line intensities toward the SDLS position by the beam dilution factors estimated in Appendix B from our IRAM 30 m and ALMA C₂H $N = 4-3$ maps. This method assumes that all rotational lines have the same spatial distribution. Table B summarizes the correction factor (f_b) applied to each line. In Sect. 5 we used the corrected line intensities to determine the best thermal pressure value, P_{th}/k_B , from isobaric PDR models (see Fig. G.1 to compare different model results).

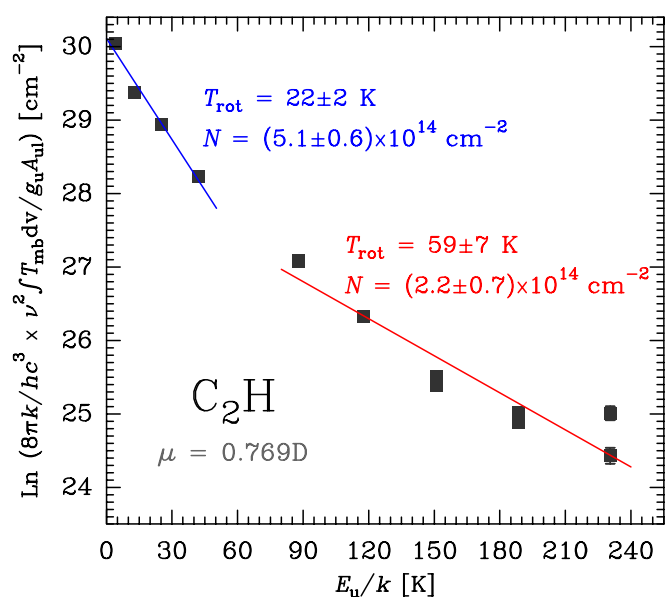


Fig. F.1. Rotational diagram of C₂H determined from IRAM 30 m (Cuadrado et al. 2015) and Herschel/HIFI (Nagy et al. 2017) observations toward the SDLS position in the Bar. We corrected the line intensities with the frequency-dependent beam-coupling factors (f_b) calculated in Sect. B. This diagram shows the fitted column density $N(C_2H)$, rotational temperature T_{rot} , and their uncertainties.

With the corrected line intensities, we constructed a rotational population diagram. The resulting diagram (Fig. F.1) can be fitted with two rotational temperature components, 22 ± 2 K and 59 ± 7 K, and $N(C_2H) = (7.3 \pm 1.3) \times 10^{14} \text{ cm}^{-2}$ (assuming Boltzmann populations and optically thin line emission). These values illustrate the excitation conditions and $N(C_2H)$ in the SDLS position. The positive curvature of the population diagram can also reflect either a single-gas-temperature, very subthermal component (with $T_{rot}(C_2H) \ll T_{64}(H_2) \approx T_k$) or a distribution of gas temperatures (e.g., Neufeld 2012) enclosed in the large beam of these single-dish observations, perhaps more consistent with the sharp temperature gradients in the PDR.

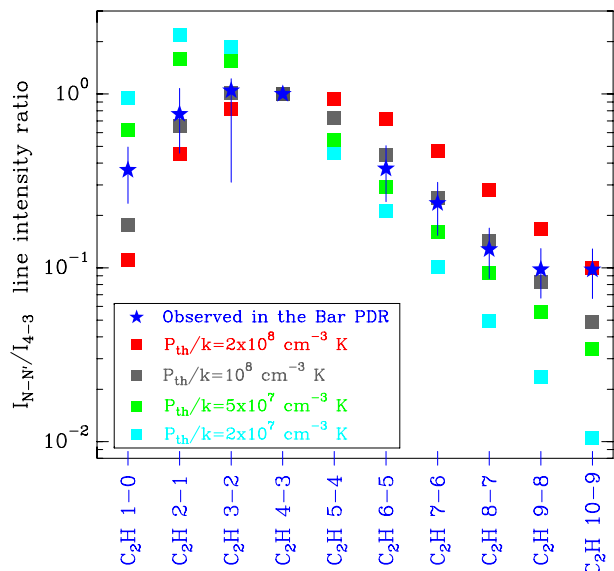


Fig. G.1. Normalized C_2H line intensities predicted by isobaric PDR models of different P_{th}/k_B . Blue stars represent the observed intensities, corrected by beam-dilution, toward the SDLS position of the Bar. Vertical lines represent the uncertainty of the observational intensity ratios.

Appendix G: P_{th} determination from C_2H lines

Here we compare the complete set of (beam-dilution corrected) C_2H $N = 1-0$ to $10-9$ intensities observed toward the SDLS position (including DF3 and DF2; Fig. 1) with isobaric PDR models of different P_{th}/k_B values. We used the output of different models: T_k , T_d , n_H , and $n(C_2H)$ profiles from $A_V = 0$ to 10 mag, as input for a nonlocal C_2H excitation and radiative transfer calculation.

The C_2H line intensities predicted by PDR models with $P_{th}/k_B = (0.5-1) \times 10^8 \text{ K cm}^{-3}$ bracket the observed line intensities. The gas thermal pressure and G_0 control the chemistry at the DF, through the production of $H_2^+(v \geq 1)$ (which triggers the formation of simple hydrocarbons, see Sect. 6.1). P_{th}/k_B sets the gas density (which drives the collisional excitation of the observed lines). Since the Bar is not a perfectly edge-on PDR, comparing absolute line intensities requires knowledge of the tilt angle α relative to a purely edge-on PDR. Thus, we compare the C_2H line intensities normalized by the C_2H $N = 4-3$ line intensity. As these rotationally excited lines are effectively optically thin (i.e., their intensities are proportional to $N(C_2H)$), the assumption of a tilt angle leads to the same geometrical intensity enhancement factor for all lines. Figure G.1 shows the predicted normalized $I(C_2H N - N')/I(C_2H 4 - 3)$ line intensities for different P_{th} values (colored squares) along with the observed line intensity ratios (blue stars). Models with $P_{th}/k_B = 2 \times 10^8 \text{ K cm}^{-3}$ produce peak abundances of $[C_2H] \approx 10^{-6}$ and gas densities that are too high. They overestimate the observed high- $N/4-3$ intensity ratios. On the other hand, models with the lowest pressure lead to much lower gas densities (several 10^4 cm^{-3}) and low $[C_2H]$ peak abundances, a few 10^{-8} . This leads to faint C_2H emission and very low high- $N/4-3$ intensity ratios. The best agreement is for models with $P_{th}/k_B \approx 10^8 \text{ K cm}^{-3}$. This should be taken as the typical pressure in the bright C_2H -emitting layers. The poorer agreement with the observed $I(C_2H 10 - 9)/I(C_2H 4 - 3)$ ratio may suggest either higher density substructures exist within the large beam enclosed by the single-dish observations (e.g., Nagy et al. 2015; Andree-Labsch et al. 2017) or additional excitation mechanisms, such as chemical formation pumping, that play a role in the excitation of C_2H excited levels.

Appendix H: Fine-structure excitation of $C(^3P)$ by H_2

Kłos et al. (2018, 2019) provided rate coefficients for the fine structure excitation of $C(^3P)$ by inelastic collisions with H_2 in the 10-100 K range. The scattering calculations were based on highly-correlated $C(^3P)-H_2$ potential energy surfaces (PESs) computed at the explicitly correlated multireference configuration interaction level of theory (Shiozaki et al. 2011) using a large atomic basis set. Quantum scattering close-coupling equations were solved using the HIBRIDON package (Alexander et al. 2023) in order to get the inelastic cross sections and rate coefficients. The spin-orbit energy levels of $C(^3P_J)$ atom are 0, 16.41671 and 43.41350 cm^{-1} for $J = 0, 1$ and 2, respectively. Details about the calculations can be found in Kłos et al. (2018, 2019).

The scattering data were compared in great detail with experimental measurement at low collisional energies (Kłos et al. 2018, 2019; Plomp et al. 2024) and a very good agreement was found. This comparison validates the high accuracy of the $C(^3P)-H_2$ PES developed and of the scattering approach used.

Here, we extend the scattering calculations to higher temperatures (up to 3000 K) in order to cover the astrophysical needs for modeling PDRs and the warm neutral medium. Scattering calculations were performed for collision energies up to $15,000 \text{ cm}^{-1}$. The close-coupling equations are propagated using hybrid Alexander-Manolopoulos propagator from the initial distance of $R = 1.0 a_0$ to $80 a_0$, R being the distances between C and the center of mass of H_2 . The cross-sections were checked for convergence with respect to the inclusion of a sufficient number of partial waves and energetically closed channels. The H_2 basis included all levels with a rotational quantum number $J \leq 6$ belonging to the ground vibrational state manifold, and the contributions of the first 200 partial waves were included in the calculations at $15,000 \text{ cm}^{-1}$. Thermal rate coefficients in $\text{cm}^3 \text{ s}^{-1}$ (Fig H.1) were obtained by an integration of the cross-sections over a Maxwell-Boltzmann distribution of the collisional energy.

We compared the new rate coefficients to those computed by Schroder et al. (1991) and frequently used in astrophysical models. The global agreement is good even if deviations of $\sim 20\%$ exist at low T . The differences can be explained by the use of different PESs and couplings between electronic states.

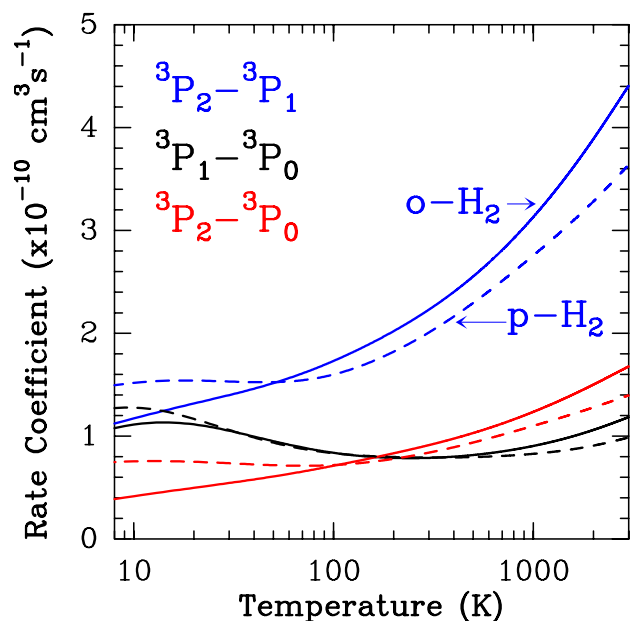


Fig. H.1. Rate coefficients for inelastic collisions between atomic carbon $C(^3P)$ and $o-H_2$ ($J=1$) (continuous curves) and $p-H_2$ ($J=0$) (dashed).